Drag reduction in wall-bounded turbulence by synthetic jet sheets

Feng Xie, Jose D. Pérez-Muñoz, Ning Qin†, and Pierre Ricco

¹Department of Mechanical Engineering, The University of Sheffield, Mappin Street, S1 3JD Sheffield, United Kingdom

A turbulent drag-reduction method employing synthetic jet sheets in a turbulent channel flow is investigated by direct numerical simulations. The jet sheets are wall-parallel and produced by periodic blowing and suction from pairs of thin slots aligned with the main streamwise flow. By varying the slot height and the jet-sheet angle with respect to the spanwise direction, drag-reduction margins between 10% and 30% are obtained for jet-sheet angles between 45° and 75°, while a drag increase of almost 100% is computed when the jet sheets are spanwise-oriented. When global skin-friction drag reduction occurs, the wall-shear stress near the jet-sheet exits increases during suction and decreases during blowing, while the velocity fluctuations weaken during suction and intensify during blowing. The global drag-reduction effect is produced by a finite counter flow induced by the nonlinear interaction between the jet-sheet flow and the main flow, although the turbulent intensity and Reynolds shear stresses increase. The power spent to generate the jet sheets is computed by numerically modelling the actuator underneath the channel flow as a piston oscillating sinusoidally along the spanwise direction in a round-shaped cavity from which the fluid is released into the channel through the cavity exits. A power balance leads to the computation of the efficiency of the actuator system, quantifying the portion of the piston power that is lost as internal-power fluxes and heat transfer through the cavity walls. For the tested configurations, the power consumed by the piston to generate the jet sheets is larger than the power saved thanks to the drag reduction.

1. Introduction

The reduction of turbulent skin-friction drag has been the subject of major interest in the fluid mechanics community for decades, due to the potential to lead to lower fuel consumption, noise, and pollutants emissions in numerous industrial and technological applications.

Amongst the active flow-control techniques, namely those requiring an external energy input, significant reductions of turbulent skin-friction drag have been achieved by applying spanwise sinusoidal wall oscillations. This drag-reduction effect was first reported in a fully developed turbulent channel flow by Jung *et al.* (1992) via direct numerical simulations (DNS). They studied the response of wall-bounded turbulence to different periods of spanwise wall oscillations, T_{osc}^+, ranging from 25 to 500, and computed a maximum 40% decrease of the wall-shear stress when the turbulence intensity was

† Email address for correspondence: n.qin@sheffield.ac.uk

suppressed the most for a period of $T_{\mathrm{osc}}^+ = 100$ (the superscript + herein indicates scaling by the wall-friction velocity).

Baron & Quadrio (1996) confirmed the drag-reduction results of Jung *et al.* (1992) by DNS and first considered the energy balance of a turbulent channel flow with spanwise wall oscillations by fixing the oscillating period for $T_{\mathrm{osc}}^+ = 100$ and changing the amplitude of the oscillation. A positive net energy balance, computed by subtracting the power spent to move the wall from the power saved through drag reduction, was found for small wall-velocity amplitudes. Choi *et al.* (1998) experimentally investigated a fully developed turbulent boundary layer subjected to spanwise wall oscillations. They confirmed the results of the previous DNS studies, and a maximum skin-friction reduction of 45% was measured at a distance of five boundary-layer thicknesses downstream of the start of oscillating section of the wall. Quadrio & Ricco (2004) also employed DNS to further investigate the power saved and the power required by the spanwise wall oscillations in a turbulent channel flow. The maximum drag-reduction margin of 45% and the maximum net energy saving of 7% were both computed for $T_{\mathrm{osc}}^+ = 125$. The drag-reduction effect and the net balance were improved by Quadrio *et al.* (2009) and Quadrio & Ricco (2011) by the use of streamwise-travelling waves of spanwise wall velocity. Backward-travelling waves always generated drag reduction, while forward-travelling waves led to drag increase when the phase speed of the waves was comparable with the convection velocity of the near-wall turbulent structures. Waves travelling forward with a small phase speed led to a maximum drag-reduction margin of 48% and a maximum net power saving of 23%. The discussed studies confirm that spanwise-wall forcing methods are promising because of the large drag-reduction margin and positive net energy balance, but their direct implementation in technological systems, such as over aircraft wings or fuselage, is undoubtedly prohibitive because of the impractical requirement of the fast and large-scale motion of the surface.

An alternative active method for drag reduction without moving walls is synthetic jets (Glezer & Amitay 2002), which involve localized zero-net-mass periodic wall transpiration. Inspired by the wall-oscillation technique, studies have focused on the alteration of wall turbulence by synthetic jets along the spanwise direction. Iuso *et al.* (2002) and Iuso & Di Cicca (2007) demonstrated experimentally that local skin-friction reductions as large as 30% can be obtained in a turbulent channel flow with pairs of jets. These jets, ejecting from ten holes drilled through the upper channel wall and produced by a compressed air supply, were alternately inclined at angles of $\pm 45°$. The holes were aligned along the spanwise direction and the measurement devices were positioned downstream of the jet-injection section. Iuso *et al.* (2002) conjectured that the drag-reduction effect was achieved by the combined action of the pairs of counter-rotating streamwise vortices generated by the jets and the local flow separation close to the location of the jet orifices. Tay *et al.* (2007) also forced the wall turbulence in a wind tunnel by jets ejecting from holes inclined at a angle of $45°$, but air was released continuously from the holes. A local drag-reduction margin of 50% was measured under the optimal condition. Cannata & Iuso (2008) and Cannata *et al.* (2020) continued the work of Iuso & Di Cicca (2007) and forced the near-wall turbulence by synthetic jets ejecting from ten tubes installed on the top part of the two vertical channel walls. The jet holes were aligned in the streamwise direction and the jet forcing was spanwise and tangential to the upper channel wall. The peak reduction of the local mean drag was 22%. Using DNS, Yao *et al.* (2018) mimicked the bulk spanwise motion caused by the spanwise synthetic jets by imposing a body force in the equations of motion. Drag reduction was achieved and the net power saving was 17% in the optimal case.

Spanwise jets have also been generated near the wall by pulsed-DC plasma actuation.

The aerodynamics research group at the University of Notre Dame demonstrated that this technique can lead to turbulent drag-reduction margins as large as 75% (Corke & Thomas 2018; Thomas *et al.* 2019). The plasma-induced jet velocity was generated in extremely short pulses by electrodes located at about 1000 wall units apart along the span. The low power spent led to a positive net power saved. Through near-wall plasma forcing, Hehner *et al.* (2019) and Hehner *et al.* (2020) produced a well-defined oscillating boundary layer that could be utilized for near-wall flow control. Ricco *et al.* (2021) reviewed the existing literature on turbulent drag reduction via spanwise actuation, including wall motion, plasma body forces and synthetic jets.

In the previous studies, jets have led to drag reduction locally in the proximity of the jet holes, but a distributed reduction of the wall-shear stress over the entire surface has not been achieved. Furthermore, only experimental studies exist on drag reduction by spanwise-oriented synthetic jets and the mechanical actuators for the generation of jets have never been modelled. The objective of the present study is therefore to investigate the effect of spanwise-oriented jets by numerical means in order to achieve drag reduction over an extended portion of the surface bounding the turbulence. To reach our objective, we employ a novel technique based on jet sheets extending continuously along the streamwise direction, instead of localized jets from orifices that have not been shown to lead to distributed drag reduction. The wall-tangential jet sheets force a fully developed turbulent channel flow at a friction Reynolds number of $Re_\tau = 180$, and are confined in the very proximity of the wall. They eject from thin slots parallel to the channel walls, oscillating sinusoidally in time.

As the jet sheets are an active flow-control method, power is required to operate them. In order to calculate the power spent, it is therefore fundamental to accurately model the actuators that generate the jet sheets. An actuator is modelled as an oscillating piston located in a cavity underneath the channel walls. The flow generated by the actuators inside the cavity is computed numerically, and the power spent is accounted for in the power budget for the computation of the net power saved. The control method is herein referred to as wall-tangential Synthetic Jet Sheets (SJS).

In §2, the flow system is described and the numerical procedures are presented. Sections 3.1, 3.2, and 3.3 discuss the results on the drag-reduction effects and the turbulent-flow physics, while the cavity flow and the power performance of the SJS actuator is studied in §3.4. The conclusions are drawn in §4.

2. Flow system and numerical procedures

In this section, the channel and the actuators are described in §2.1 and the averaging procedures are discussed in §2.2. Appendix A presents a validation study of the numerical computations.

2.1. *Channel flow and actuators*

We numerically study a fully developed turbulent channel flow of air driven at a constant mass flow rate and at a friction Reynolds number $Re_\tau = u_\tau^* h^* / \nu_c^* = 180$, where h^* is the half-channel height and $u_\tau^* = \sqrt{\tau_w^*/\rho_c^*}$ is the wall-friction velocity (the superscript * herein denotes dimensional quantities). The quantities τ_w^*, ν_c^* and ρ_c^* are the space- and time-averaged wall-shear stress in the uncontrolled case, the kinematic viscosity and the density of air, respectively. Quantities that are not marked by any symbol are scaled in outer units, i.e., by h^* and U_p^*, the centreline velocity of the laminar parabolic Poiseuille flow at the same mass flow rate, and quantities marked
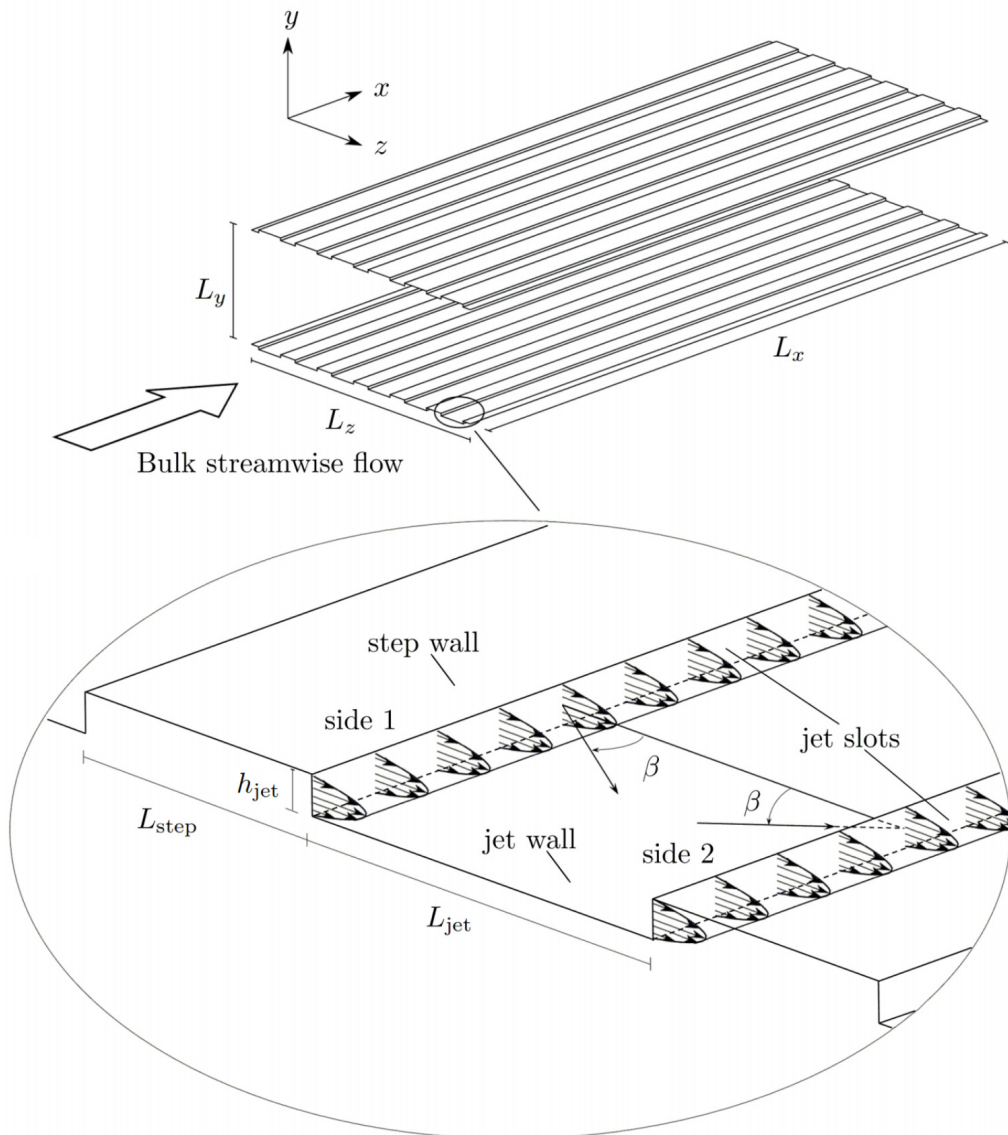
Figure 1: Schematic of the channel flow with SJS. The velocity profiles are for $\beta = 0°$.

by the superscript '+' are non-dimensionalized in wall units, i.e., by ν_c^* and u_τ^* of the uncontrolled case.

Figure 1 shows the flow system, where L_x, L_y and L_z are the lengths of the computational domain in the streamwise, wall-normal and spanwise directions, respectively. The flow conditions and dimensions of the flow cases discussed in the main text are given in table 1. Appendix B presents additional flow cases. On each wall, six steps of height h_{jet} are aligned along the streamwise direction. The SJS eject from slots located at both sides of the steps. The surface of the step is named 'step wall' and the surface between two slots is named 'jet wall'. The spanwise width of a step wall is L_{step} and the spanwise width of a jet wall is L_{jet}. The length L_{jet}^+ has been chosen to be comparable with the spacing

Parameters	Smooth channel	Controlled channel
$L_x \times L_y \times L_z$	$2\pi \times 2 \times 4\pi/3$	$2\pi \times 1.98 \times 4\pi/3$
$h_{\mathrm{jet}} \times L_{\mathrm{step}} \times L_{\mathrm{jet}}$	$0 \times 0.199 \times 0.499$	$0.011 \times 0.199 \times 0.499$
$L_x^+ \times L_y^+ \times L_z^+$	$1131 \times 360 \times 754$	$1131 \times 357 \times 754$
$h_{\mathrm{jet}}^+ \times L_{\mathrm{step}}^+ \times L_{\mathrm{jet}}^+$	$-$	$2 \times 35.9 \times 89.8$
Number of devices N_d	0	12

Table 1: Flow conditions and dimensions of the flow cases discussed in the main text. Appendix B presents additional flow cases.

of the low-speed streaks in wall-bounded turbulence (about 100 units) and L_{step}^+ has been chosen as small as possible not to disrupt the flat-wall standard geometry, but wide enough so that it could realistically accommodate the channels underneath the steps, through which air flows to discharge into the main turbulent flow. A suction/blowing type boundary condition is applied at the slot exits. The skin friction of the flow through the smooth channel without steps on the walls is taken as the reference value for the computation of the drag reduction. The terminology 'SJS off' refers to the channel flow with steps but without SJS actuation, while 'SJS on' refers to the channel flow with steps and activated SJS.

The components of the SJS velocity vector at the slot exits are

$$u_{\mathrm{jet}} = U_{\mathrm{jet}} \sin\beta \sin\left(\frac{2\pi t}{T_{\mathrm{osc}}}\right), \qquad (2.1)$$

$$v_{\mathrm{jet}} = 0, \qquad (2.2)$$

$$w_{\mathrm{jet}} = U_{\mathrm{jet}} \cos\beta \sin\left(\frac{2\pi t}{T_{\mathrm{osc}}}\right), \qquad (2.3)$$

where u, v and w are the velocity components along the streamwise, wall-normal and spanwise directions, respectively. The angle β of the SJS ejection is defined with respect to the spanwise direction and the period of the oscillation is $T_{\mathrm{osc}}^+ = 125$. The SJS work in pairs as shown in figure 1, i.e., the SJS velocities are $u_{\mathrm{jet,side1}} = -u_{\mathrm{jet,side2}}$ and $w_{\mathrm{jet,side1}} = w_{\mathrm{jet,side2}}$.

The velocity profile U_{jet} follows a parabolic function (You *et al.* 2006),

$$U_{\mathrm{jet}} = U_{\mathrm{jet,peak}} \left[1 - \left(\frac{2y_{\mathrm{jet}}}{h_{\mathrm{jet}}} - 1\right)^2\right], 0 \leqslant y_{\mathrm{jet}} \leqslant h_{\mathrm{jet}}, \qquad (2.4)$$

where $U_{\mathrm{jet,peak}}$ is the peak velocity and y_{jet} is the wall-normal distance from the jet wall. The peak velocity is $U_{\mathrm{jet,peak}}^+ = 27$ for the main cases studied. The Reynolds number and the Strouhal number of the SJS flow are $Re_{\mathrm{jet}} = U_{\mathrm{jet,peak}}^* h_{\mathrm{jet}}^* / \nu_c^* = 54$ and $St = h_{\mathrm{jet}}^* / (U_{\mathrm{jet,peak}}^* T_{\mathrm{osc}}^*) = 0.0006$. The Mach number based on the channel-flow bulk velocity and the speed of sound at the reference temperature is 0.21. The Mach number based on the peak SJS velocity and the speed of sound at the reference temperature is 0.35.

2.2. *Averaging procedures*

The case with the SJS off is used as the initial flow for the SJS simulations. When this turbulent flow has reached fully developed statistically convergent conditions, the SJS are switched on. The flow in turn evolves to a new drag-reducing or drag-increasing regime.

The averaging procedures are performed on a quantity after discarding the transient from the beginning of the SJS actuation, when the flow has reached fully developed conditions.

The flow within the computational domain is statistically periodic along the spanwise direction. The minimal geometrical flow unit that repeats itself along the spanwise direction is $L = L_{\text{step}} + L_{\text{jet}}$. As the flow is statistically homogeneous along x, the spatial ensemble and streamwise average of a quantity q is

$$[q]_e(y, z_e, t) = \frac{1}{n_z L_x} \sum_{n_z=0}^{N_z-1} \int_0^{L_x} q(x, y, z_e + n_z L, t) \, \mathrm{d}x, \qquad (2.5)$$

where $0 \leqslant z_e \leqslant L$ is the ensemble spatial coordinate and N_z is the number of minimal geometrical units in the computational domain.

As the SJS forcing is sinusoidal with period T_{osc}, the flow is statistically periodic with the same period. The phase ensemble average is

$$\langle q \rangle(y, z_e, \varphi) = \frac{1}{N_{\text{osc}}} \sum_{n_{\text{osc}}=0}^{N_{\text{osc}}-1} [q]_e \left[y, z_e, \left(\frac{\varphi}{2\pi} + n_{\text{osc}} \right) T_{\text{osc}} \right], \qquad (2.6)$$

where N_{osc} is the number of oscillating periods and φ is the phase,

$$\varphi = \frac{2\pi\tau}{T_{\text{osc}}}, \quad (0 \leqslant \tau \leqslant T_{\text{osc}}). \qquad (2.7)$$

The ensemble and time average over a time interval T is

$$\bar{q}(y, z_e) = \frac{1}{T} \int_0^T [q]_e(y, z_e, t) \mathrm{d}t. \qquad (2.8)$$

A triple decomposition is defined as

$$q(x, y, z, t) = \bar{q}(y, z_e) + \tilde{q}(y, z_e, \varphi) + q''(x, y, z, t), \qquad (2.9)$$

where

$$\tilde{q}(y, z_e, \varphi) = \langle q \rangle(y, z_e, \varphi) - \bar{q}(y, z_e) \qquad (2.10)$$

is the periodic fluctuation induced by the SJS and

$$q''(x, y, z, t) = q(x, y, z, t) - \langle q \rangle(y, z_e, \varphi) \qquad (2.11)$$

denotes a purely turbulent quantity. The total fluctuation is defined as

$$q'(x, y, z, t) = \tilde{q}(y, z_e, \varphi) + q''(x, y, z, t). \qquad (2.12)$$

The total Reynolds shear stresses are computed by the total fluctuations, $\overline{u'v'}$, while the Reynolds shear stresses involving only the turbulent fluctuations are computed as $\overline{u''v''}$. The scaled wall-shear stress is

$$C_f(x, z, t) = \frac{2\mu_c^*}{\rho_c^* U_b^{*2}} \frac{\partial u^*(x, y, z, t)}{\partial y^*} \bigg|_{y^*=0}, \qquad (2.13)$$

where μ_c^* is the dynamic viscosity of air and U_b^* is the bulk mean velocity. The spatially averaged skin-friction coefficient is

$$\hat{C}_f(t) = \frac{1}{L_z L_x} \int_0^{L_z} \int_0^{L_x} C_f(x,z,t) \mathrm{d}x \mathrm{d}z. \tag{2.14}$$

The time and spatially ensemble averaged skin-friction coefficient in the period T_{osc} is

$$\overline{C}_f(z_e) = \frac{1}{N_z T_{\mathrm{osc}} L_x} \sum_{n_z=0}^{N_z-1} \int_0^{T_{\mathrm{osc}}} \int_0^{L_x} C_f\left(x, z_e + n_z L, \tau\right) \mathrm{d}x \mathrm{d}\tau. \tag{2.15}$$

The phase and spatially ensemble averaged skin-friction coefficient is

$$\langle C_f \rangle (z_e, \varphi) = \frac{1}{N_z N_{\mathrm{osc}} L_x} \sum_{n_z=0}^{N_z-1} \sum_{n_{\mathrm{osc}}=0}^{N_{\mathrm{osc}}-1} \int_0^{L_x} C_f\left[x, z_e + n_z L, \left(\frac{\varphi}{2\pi} + n_{\mathrm{osc}}\right) T_{\mathrm{osc}}\right] \mathrm{d}x. \tag{2.16}$$

The level of gross drag reduction is defined as

$$\mathcal{R}(\%) = 100(\%) \cdot \frac{[C_f]_{\mathrm{smooth}} - [C_f]_{\mathrm{controlled}}}{[C_f]_{\mathrm{smooth}}}, \tag{2.17}$$

where $[C_f]$ is the global skin-friction coefficient,

$$[C_f] = \frac{1}{T L_z L_x} \int_0^T \int_0^{L_z} \int_0^{L_x} C_f(x,z,t) \mathrm{d}x \mathrm{d}z \mathrm{d}t. \tag{2.18}$$

2.3. *Numerical solver*

The in-house flow solver SHEFFlow, based on and further developed from the solver by Qin & Xia (2008), is utilized to simulate the turbulent channel flow and the flow in the cavity underneath the channel. It solves the three-dimensional compressible Navier-Stokes equations by employing a finite volume method, a dynamic mesh formulation, and a preconditioned Roe scheme. For the spatial discretization, a fifth-order MUSCL scheme (Monotonic Upwind Scheme for Conservation Laws) without any limiter functions is employed to gain higher order of accuracy and low dissipation (Kim & Kim 2005). A dual time-step scheme is used for the temporal discretization (Weiss & Smith 1995). The physical-time term is discretized implicitly by a second-order accurate, three-point backward finite-difference scheme, while the pseudo-time derivative is driven to zero by a multistage Runge-Kutta scheme. Parallelization is achieved using the Open Message Passing Interface.

3. Results

3.1. *Turbulent drag reduction*

Figure 2 displays the time evolution of the spatially averaged skin-friction coefficient $\hat{C}_f$ for different SJS angles β. The coefficient is strongly influenced by the SJS: it displays intense fluctuations that become periodic after two forcing periods. The oscillating period of these wall-friction fluctuations is $T^+_{\mathrm{osc},\hat{C}_f} = 62.5$, half of the period T_{osc} of the SJS. The fluctuations of $\hat{C}_f$ depend on the SJS velocity: they are smallest for $\beta = 0°$ and largest for $\beta = 60°$, which means that they increase as the streamwise component of the SJS velocity vector increases up $\beta = 60°$. For larger angles, the fluctuating amplitude does not grow monotonically with the SJS angle: the case of $\beta = 75°$ has a smaller amplitude than the case of $\beta = 60°$. As β approaches 90°, the SJS flow becomes more and more
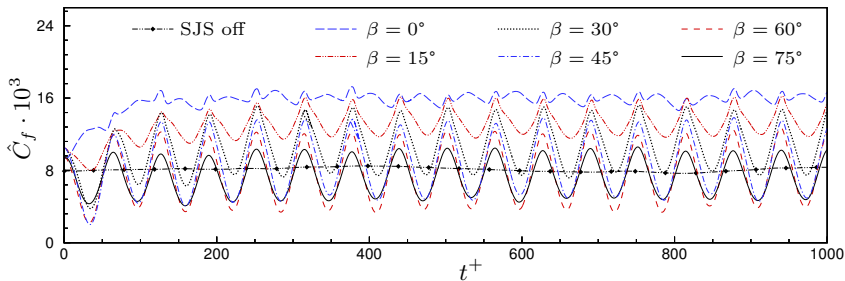
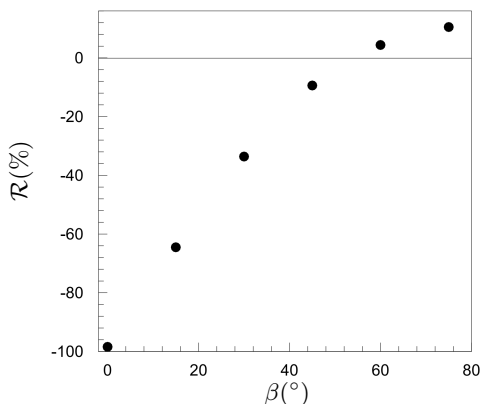Figure 2: Time evolution of the skin-friction coefficient for different SJS angles.

Figure 3: Drag reduction for different SJS angles.

aligned along the streamwise direction, so that the area of influence of the SJS becomes smaller, leading to a small fluctuating amplitude of $\hat{C}_f$. The amplitude of the wall-shear stress therefore oscillates less for large β values than for $\beta = 60°$. When $\beta = 90°$, no flow exhausts into the channel from the SJS exits because the SJS velocity vector is unrealistically parallel to the slots, thus being less able to influence the bulk flow.

Figure 3 shows the drag-reduction margin as a function of the SJS angle. The maximum value is $\mathcal{R} = 10.5\%$ when $\beta = 75°$. The SJS angle $\beta = 0°$ gives the maximum drag increase, that is, the drag coefficient is 98.4% larger than the coefficient of the uncontrolled channel. Interpolating the data in figure 3 leads to the estimate that SJS with $\beta = 54°$ generate a flow with the same average drag as the uncontrolled flow. Appendix B discusses the effects of varying the slot height, the period of forcing, the peak SJS velocity and the distance between the slots.

3.2. *Mean-flow and turbulence statistics*

Figure 4(a) illustrates the time and spatially averaged streamwise-velocity $\overline{u}^+$ near the slots for the reference case with the SJS off, the drag-increase case for $\beta = 0°$, and the drag-reduction case for $\beta = 75°$. The skin-friction coefficient of the case with SJS off is $\hat{C}_f = 8.20 \cdot 10^{-3}$ for the parameters in table 1, i.e. 0.24% larger than that of the smooth channel, $\hat{C}_f = 8.18 \cdot 10^{-3}$ (Kim *et al.* 1987). As reported in Appendix A, this difference is within the uncertainty range, estimated to be less than 1%, which proves that the
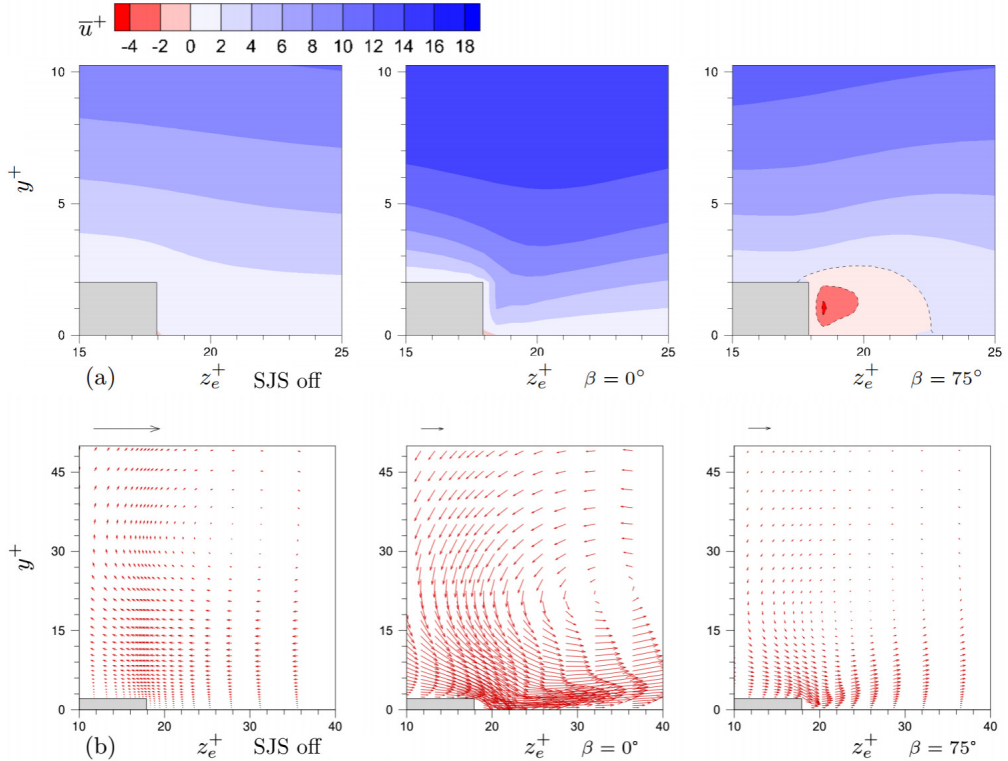
Figure 4: Time and spatially averaged flow near the slots on the $y-z$ plane. (a) Contours of the averaged streamwise-velocity. (b) The vectors of the induced time-averaged flow $(\overline{v}^+, \overline{w}^+)$. The magnitude of the velocity vectors is equal to $\sqrt{\overline{v}^{+2} + \overline{w}^{+2}}$. The arrows at the top of the graphs denote the unit lengths for the vectors in the corresponding graphs. The maximum magnitudes in the cases with the SJS off, $\beta = 0°$ and $\beta = 75°$ are 0.08, 3.57 and 0.56, respectively.

steps have a negligible influence on the skin friction for $h_{jet}^+ = 2$. A region of negative mean streamwise velocity is found near the slots for the case of $\beta = 75°$, which is not present when the SJS eject at $\beta = 0°$. Although the SJS are characterized by a zero net mass flux at the slots, the time averaging reveals that a significant near-wall counter flow opposite to the bulk streamwise flow occurs when $\beta = 75°$. No net counter flow is detected for $\beta = 0°$ because no SJS flow is imposed against the bulk flow. The generation of the counter flow near the SJS slots is similar to that induced by canonical synthetic jets exhausting perpendicularly to a cross flow. In their review, Glezer & Amitay (2002) discuss several cases where synthetic jets, although characterized by a net zero mass flux, modify the cross flow into which they discharge and produce a displacement of its streamlines, thereby engendering a virtual change in the surface shape. In our study, the distortion of the bulk turbulent flow also occurs along the wall-normal direction as in Glezer & Amitay (2002), but the change is due to the SJS forcing, which is parallel to the walls. Increasing the SJS angle from $\beta = 0°$, the SJS flow is directed against the main flow, producing the counter flow near the exits. When the SJS angle is large enough, the counter flow becomes a dominant effect on altering the velocity profile to reduce the near-wall velocity gradient and therefore the friction drag.

Figure 4(b) shows the velocity vectors of the time-averaged cross-flow velocity components $(\overline{v}^+, \overline{w}^+)$. A mild cross flow with clockwise rotation occurs when the SJS are off, similar to the secondary flows reported by Hwang & Lee (2018) numerically and Vanderwel & Ganapathisubramani (2015) experimentally for turbulent flows over longitudinal rectangular roughness elements. Hwang & Lee (2018) systematically changed the spanwise distance and the width of the steps, and reported that the strength of the secondary vortices increases when the spanwise distance increases or when the width decreases. Vanderwel & Ganapathisubramani (2015) also revealed that the vortical flows exist next to the roughness elements and their strength depends on their spanwise spacing. When the spacing is comparable with the boundary-layer thickness, the secondary vortices reach their maximum strength. The presence of instantaneous secondary flows was further demonstrated by Vanderwel *et al.* (2019), using both experiments and numerical simulations.

When the SJS are on, although the time-averaged velocity components are null at the slots, a finite time-averaged cross flow is generated by the nonlinear interaction between the SJS and the bulk streamwise flow. The intensity of this cross flow is much larger than that in the reference case with SJS off and the rotation is anti-clockwise, that is, opposite to the rotation occurring when the SJS are off. When $\beta = 0°$, the time-averaged SJS flow is more intense and more confined near the jet wall than in the case of $\beta = 75°$. The bulk of the cross flow is pushed upwards and away from the slots. The time-averaged cross flow is similar to the wall jets studied by Yao *et al.* (2018), although in their case finite time-averaged jets are expected to form because they are generated by a steady spanwise body force.

Figure 5 further compares time and spatially averaged quantities for the cases with the SJS off, $\beta = 0°$ and $\beta = 75°$. Figure 5(a) shows the averaged scaled wall-shear stresses $\overline{C}_f$ along the spanwise direction. Consistently with the near-wall counter flow observed for $\beta = 75°$ near the slots, the local wall-friction drag is reduced there. This result proves that the drag-reduction mechanism is different from other spanwise-forcing techniques, such as the oscillation wall (Quadrio & Ricco 2004) or the streamwise-travelling waves of spanwise wall velocity (Quadrio *et al.* 2009), for which the wall-shear stress is never negative. As the case with $\beta = 75°$ involves a significant oscillatory velocity component along the streamwise direction, the drag-reduction effect is akin to that reported by Zhou & Ball (2008), who moved the wall obliquely with respect to the streamwise direction. They concluded that, although forcing the flow purely along the spanwise direction led to the best performance, drag reduction was also found when most of the wall motion was along the streamwise direction. For $\beta = 0°$, the wall-friction drag is more than six times larger than the uncontrolled value in the proximity of the slots and the wall-shear stress is not reduced at any spanwise location. Along the central part of the jet wall, the trends of the wall-shear stress are flat and overlap in all three cases, indicating that the friction drag is unaffected along that portion of the wall because that region is too far from the SJS slots. Drag increase occurs over the step walls in both controlled cases.

The profiles of the time-averaged streamwise velocity are shown in figure 5(c) and the respective spanwise locations are indicated in figure 5(b). Over the step wall at $z_e^+ = 0.1$ and 17, the large mean velocity in the controlled cases, which causes the local drag increase shown in figure 5(a), is only limited very close to the wall as the profiles show a good agreement with the uncontrolled profile at wall-normal distances $y^+ > 10$ from the step wall. The SJS with $\beta = 0°$ create drag increase near the slot at $z_e^+ = 20$ by intensifying the mean streamwise velocity only up to $y^+ = 25$, while the reverse flow for $\beta = 75°$ is confined up to $y^+ = 5$, i.e., in the viscous sublayer. At higher locations, the profiles for the controlled flows agree more closely to the uncontrolled profile, although a
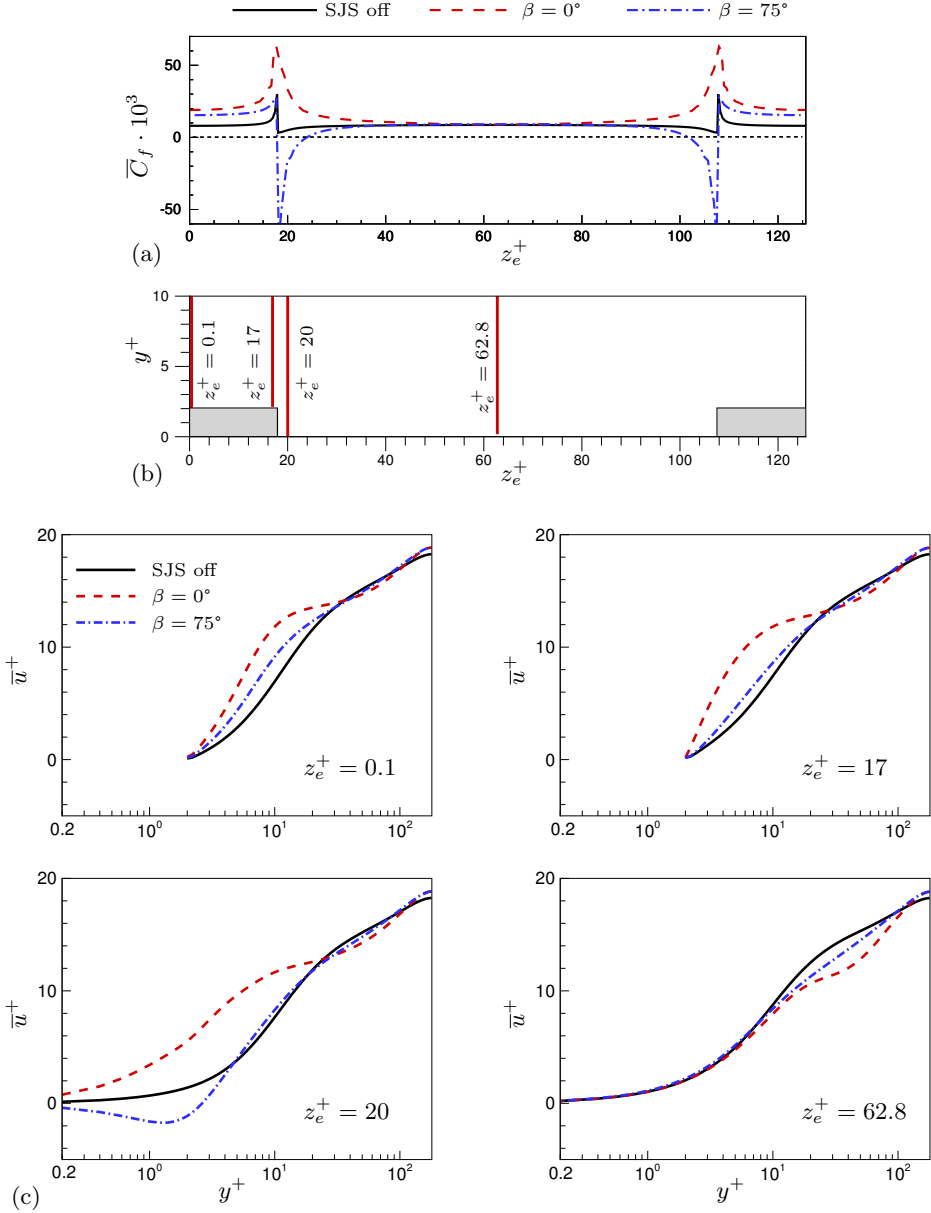
Figure 5: Comparisons of time and spatially averaged quantities at different spanwise positions. (a) The distributions of averaged skin friction along span. (b) The profile positions. (c) The profiles of averaged streamwise-velocity, covering the height range of a half channel.

velocity deficit is found for $25 < y^+ < 80$. In the middle of the jet wall at $z_e^+ = 62.8$, the three profiles overlap within the viscous sublayer and the velocity deficit with respect to the uncontrolled case between $10 < y^+ < 100$ is more pronounced than that at other spanwise locations, arguably because of the intense lift-up effect observed when the flow is time averaged, as shown in figure 4(b). This deficit of mean streamwise velocity is
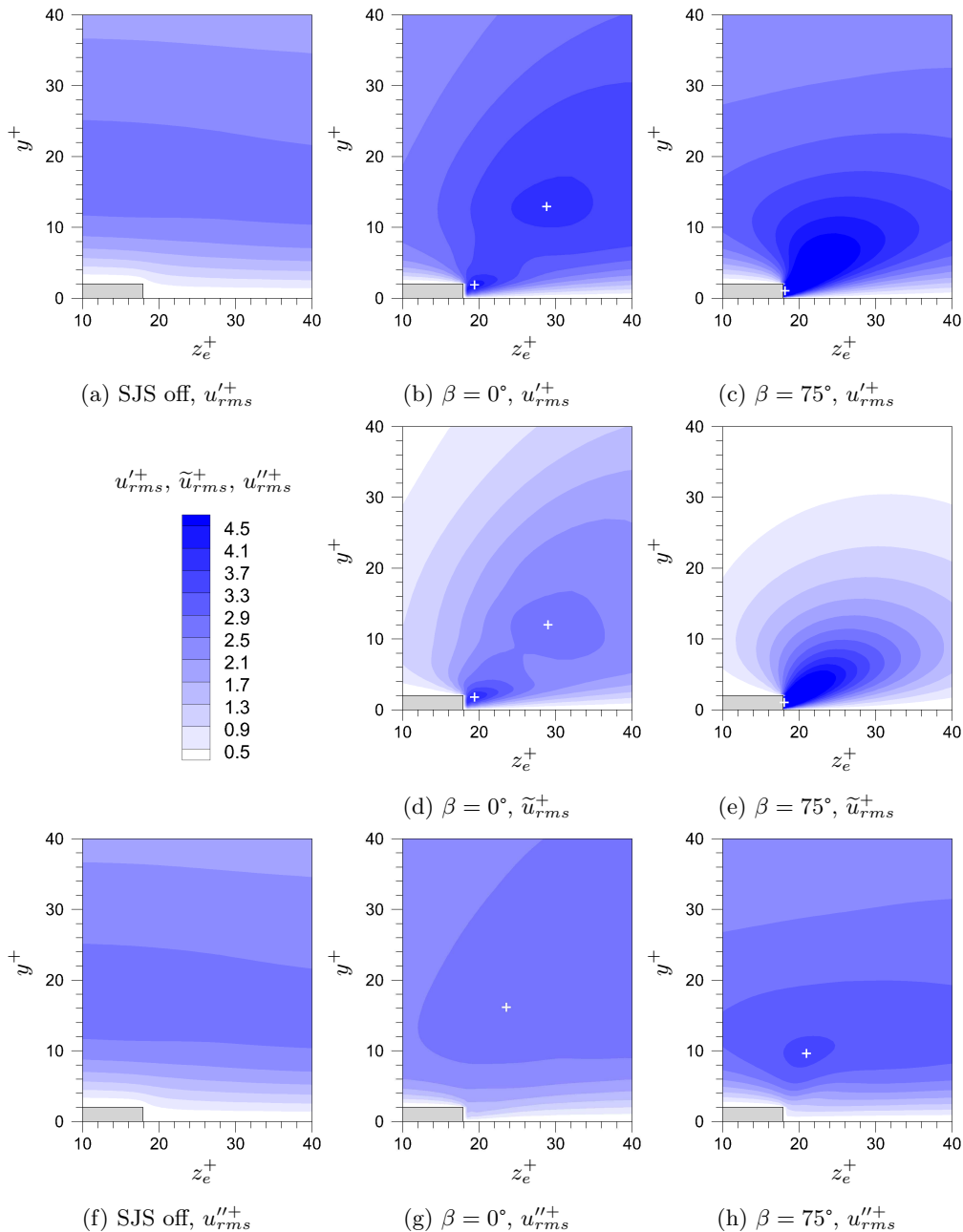
Figure 6: Contours of root mean squares of the streamwise velocity fluctuations, u'^{+}_{rms}, $\widetilde{u}^{+}_{rms}$, and u''^{+}_{rms} in the $y-z$ view. The local peak positions are denoted by the white crosses.

indeed more intense for $\beta = 0°$ than for $\beta = 75°$ because the upward flow between the slots is more significant when the SJS are spanwise only, as the middle graph of figure 4(b) illustrates.

Figure 6 shows the contour plots of the root mean squares (r.m.s.) of the streamwise
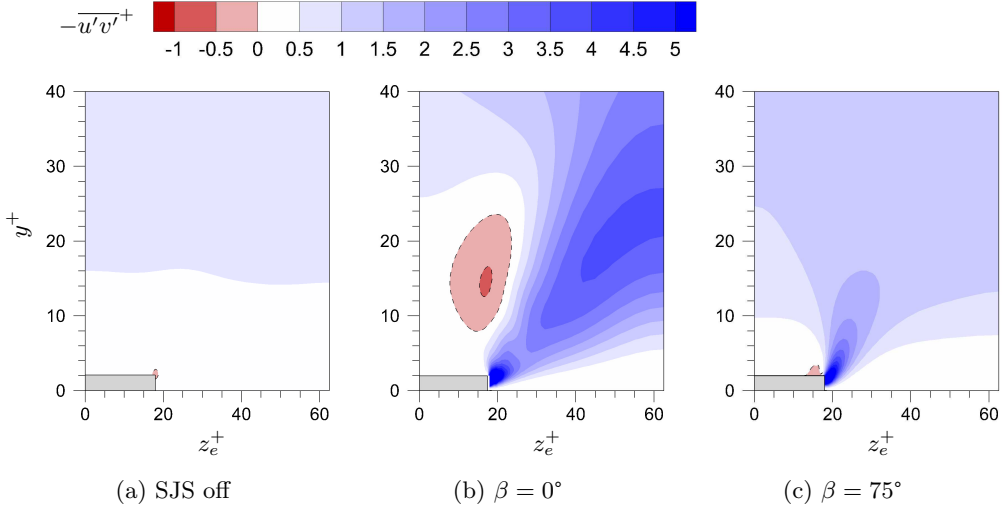
Figure 7: Contours of $-\overline{u'v'}^{+}$ in the $y-z$ plane. In this figure and in figures 9 and 10, the dashed lines denote negative values.

velocity fluctuations. Profiles in the top, middle and bottom rows refer to the total, periodic and turbulent fluctuations, respectively, as defined in (2.9). In the contours 6(a), 6(b) and 6(c) for the total fluctuations, two local peaks occur for $\beta = 0°$, the most energetic one located in the proximity of the slot. Only one local peak is computed for $\beta = 75°$, at the slot. The positions of these local peaks are the same as those of the periodic fluctuations caused by the SJS, shown in the contours 6(d) and 6(e). The periodic fluctuations are most intense for $\beta = 75°$ because part of the SJS velocity component is aligned along the streamwise direction. The periodic forcing becomes weaker at locations further away from the SJS slots because the streamwise velocity fluctuates the most near the SJS slots, causing only one local peak. For $\beta = 0°$, the streamwise velocity of SJS is zero at the SJS slots, so no additional streamwise velocity fluctuations is found. During the blowing phase, large near-wall velocity against the main channel flow is generated near the slot exit. However, during the suction phase near the slot exit, the streamwise velocity component is enhanced near the wall. These opposite behaviours lead to the local peak of the fluctuation that is closer to the slot. The other peak is only induced by the blowing SJS because the influenced region by the blowing SJS is larger than that by the suctioning SJS. As the locations of influence of blowing and suctioning are different, the fluid motions lead to two local peaks of the periodic fluctuations. Moreover, it is evident that the lift-up effect of the SJS occurs as soon as they discharge from the orifices. The periodic fluctuations are more energetic than the turbulent fluctuations, although the latter grow with respect to the uncontrolled case, as depicted in the contours 6(g) and 6(h).

Figure 7 shows that the Reynolds shear stresses $-\overline{u'v'}^{+}$, given by the total fluctuations, are increased by the SJS. In both controlled cases, $\beta = 0°$ and 75°, larger Reynolds-stress values than with the SJS off occur near the slots. The Reynolds-stress values in the SJS cases are comparable near the slot, but for $\beta = 0°$ large values are found above $y^{+} = 15$ between the slots. The case for $\beta = 0°$ also presents a region of Reynolds stress of opposite sign, centered at $y^{+}=12$ from the edge of the step wall. In the region where the Reynolds-stress values are negative, the time and spatially-averaged flow moves down

(a) 3D, $\beta = 0°$

(b) 2D, $\beta = 0°$

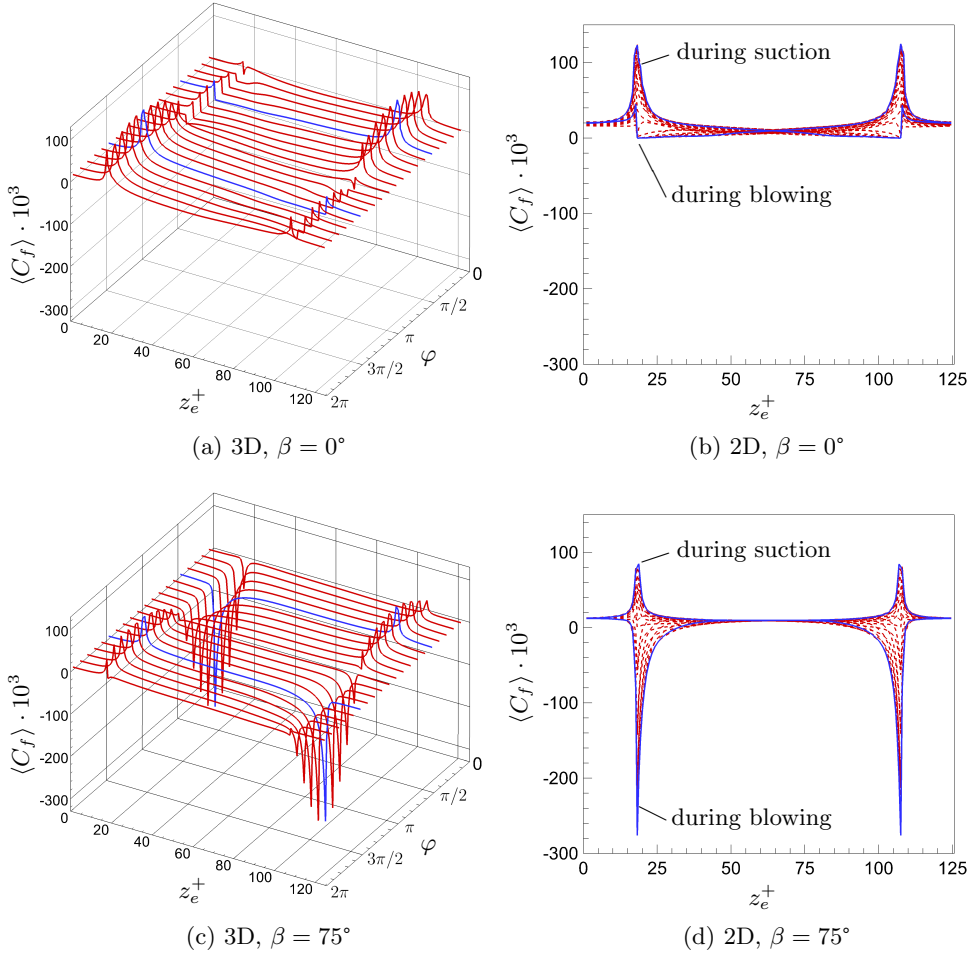(c) 3D, $\beta = 75°$

(d) 2D, $\beta = 75°$

Figure 8: Distributions of the phase and spatially ensemble averaged skin-friction coefficient. The blue lines denote the profiles at phases $\varphi = \pi/2$ or $3\pi/2$.

towards the steps, as shown in figure 4. The low-speed region of streamwise velocity is generated by the blowing SJS and gives a negative u', while, when this part of flow is accelerated upwards, which has a positive v', a region with negative $\overline{u'v'}$ is created. In the region where $\overline{u'v'}$ is positive, the flow motion in the wall-normal direction is opposite to that in the region of negative sign, although the flow motion is also in the streamwise direction.

The phase and spatially ensemble averaged skin-friction coefficients are significantly influenced by the SJS, as shown in figure 8. Fluid is blown out from the left slot and is drawn in at the right slot from $\varphi = 0$ to π, while the opposite occurs in the other half period. In both cases, $\beta = 0°$ and $\beta = 75°$, and near the slots, the wall-friction drag is reduced during blowing and increased during suction. The drag is never negative for $\beta = 0°$, while it is significantly decreased and becomes negative for $\beta = 75°$. The integral of the reduced drag offsets the integral of the raised drag for $\beta = 75°$, so an overall drag reduction is obtained.

The phase and spatially ensemble-averaged streamwise velocity $\langle u \rangle^+$ in the near-wall
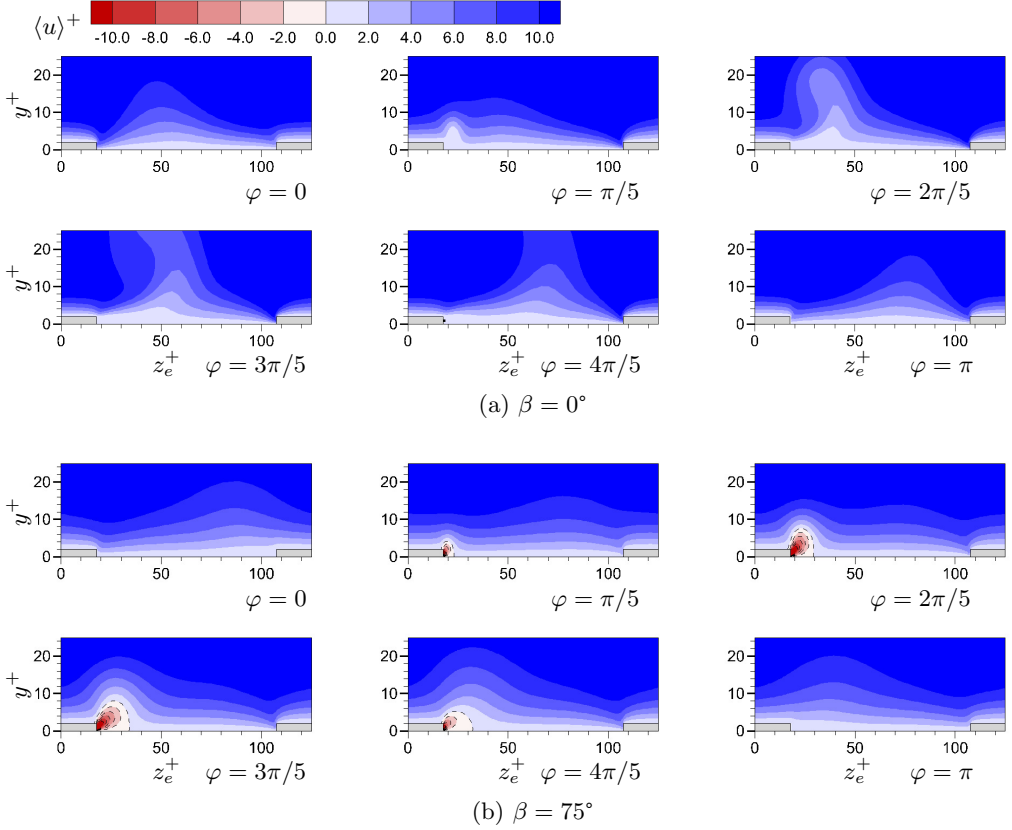
Figure 9: Contours of phase and spatially averaged streamwise velocities $\langle u \rangle^+$ in the $y - z$ plane at different phases for the cases of $\beta = 0°$ and $75°$.

region is shown in figure 9 for half the period. The blowing from the left slot influences the streamwise velocity to larger wall-normal distances than the suction from the right slot. Fluid with small streamwise velocity is blown upwards by the left SJS, while fluid with large streamwise velocity is brought downwards by the right SJS. The former reduces drag, while the latter increases it. The SJS blowing with $\beta = 0°$ influence the flow to larger wall-normal locations than the SJS blowing with $\beta = 75°$. The counter flow is generated by the SJS with $\beta = 75°$ during blowing, as depicted at $\varphi = 3\pi/5$.

Figure 10 shows the contour plots of the Reynolds shear stresses $-\langle u''v'' \rangle^+$ given by the purely turbulent fluctuations for $\beta = 0°$ and $\beta = 75°$ from $\varphi = 0$ to $\varphi = \pi$. The Reynolds shear stresses are enhanced by blowing, while the drag is decreased. Both positive and negative values of $-\langle u''v'' \rangle^+$ are produced by the blowing region of the SJS for $\beta = 0°$. The region with negative values of $-\langle u''v'' \rangle^+$ is closer to the steps than the region with positive values. For $\beta = 75°$, the positive values of $-\langle u''v'' \rangle^+$ dominate the flow field, while the region with negative values is negligible. As shown by the contours of $\overline{u'v'}^+$ and $\langle u''v'' \rangle^+$ in figures 7 and 10, large values of $\overline{u'v'}^+$ occur near the slots, while the values of $\langle u''v'' \rangle^+$ are low, indicating that the periodic velocity fluctuations contribute the most to the total Reynolds shear stress there.

The overall picture is therefore that the SJS cause drag reduction for $\beta = 75°$ through the intense near-wall counter flow being larger than the forward flow occurring in the
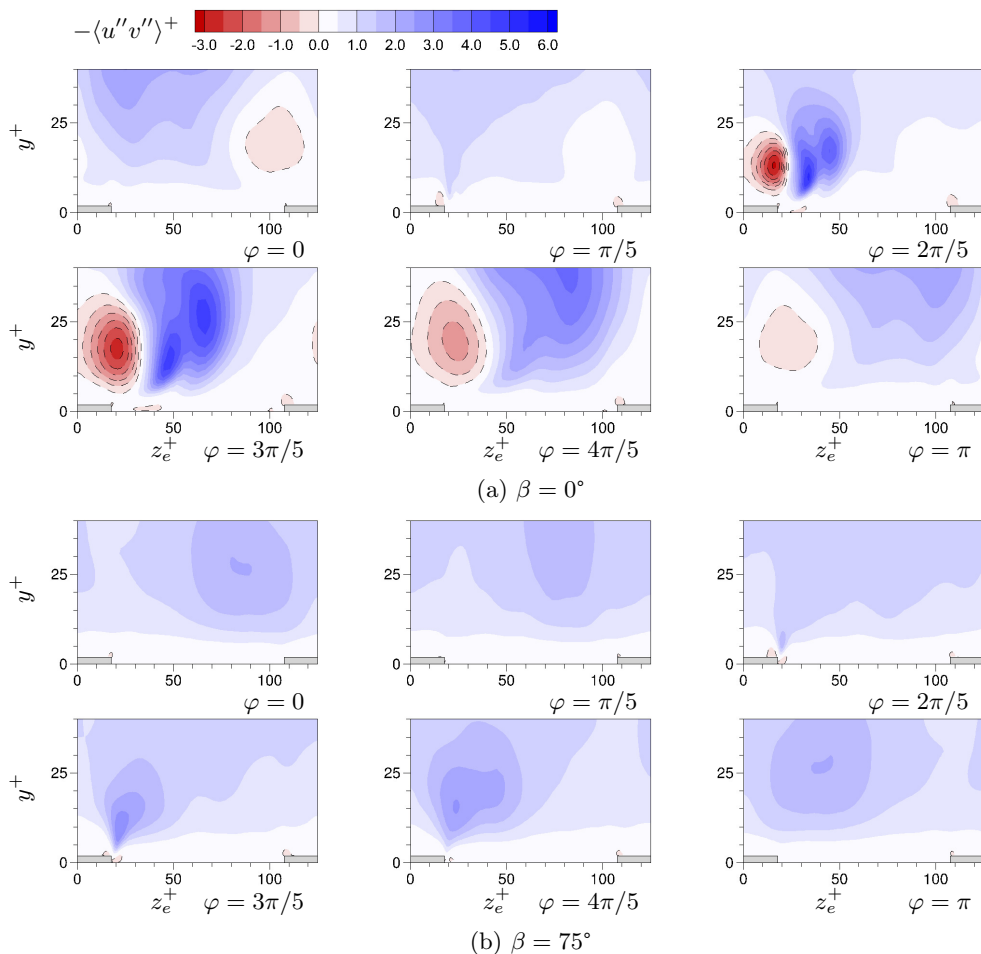
Figure 10: Contours of the Reynolds shear stress $-\langle u''v''\rangle^+$ in the $y-z$ plane at different phases for the cases of $\beta = 0°$ and $75°$.

near-wall region in the proximity of the SJS slots, despite the intensified Reynolds shear stresses. The drag-increasing case for $\beta = 0°$ also enhances the Reynolds shear stresses, but it does not benefit from the counter flow because the SJS are aligned along the spanwise direction only.

3.3. *Turbulent-flow structures*

Instantaneous flows for the cases with $\beta = 0°$ and $75°$ are discussed in this section. Figure 11 shows the isosurfaces of $\lambda_2^+ = -2$ in the bottom half-channel at different phases. The λ_2 technique to detect the vortex cores was developed by Jeong & Hussain (1995). The flows altered by the SJS display more intense vortical structures than the case without SJS forcing, irrespectively to whether the drag reduces or increases. The response of the flow to the forcing is therefore different from other spanwise forcing methods, such as streamwise-travelling waves of spanwise wall velocity (Quadrio *et al.* 2009; Quadrio & Ricco 2011), which lead to a less intense and more sporadic population of near-wall vortical structures accompanied by a reduction of wall-friction drag. Vortical

(a) SJS off

(b) $\beta = 0°$

(c) $\beta = 75°$
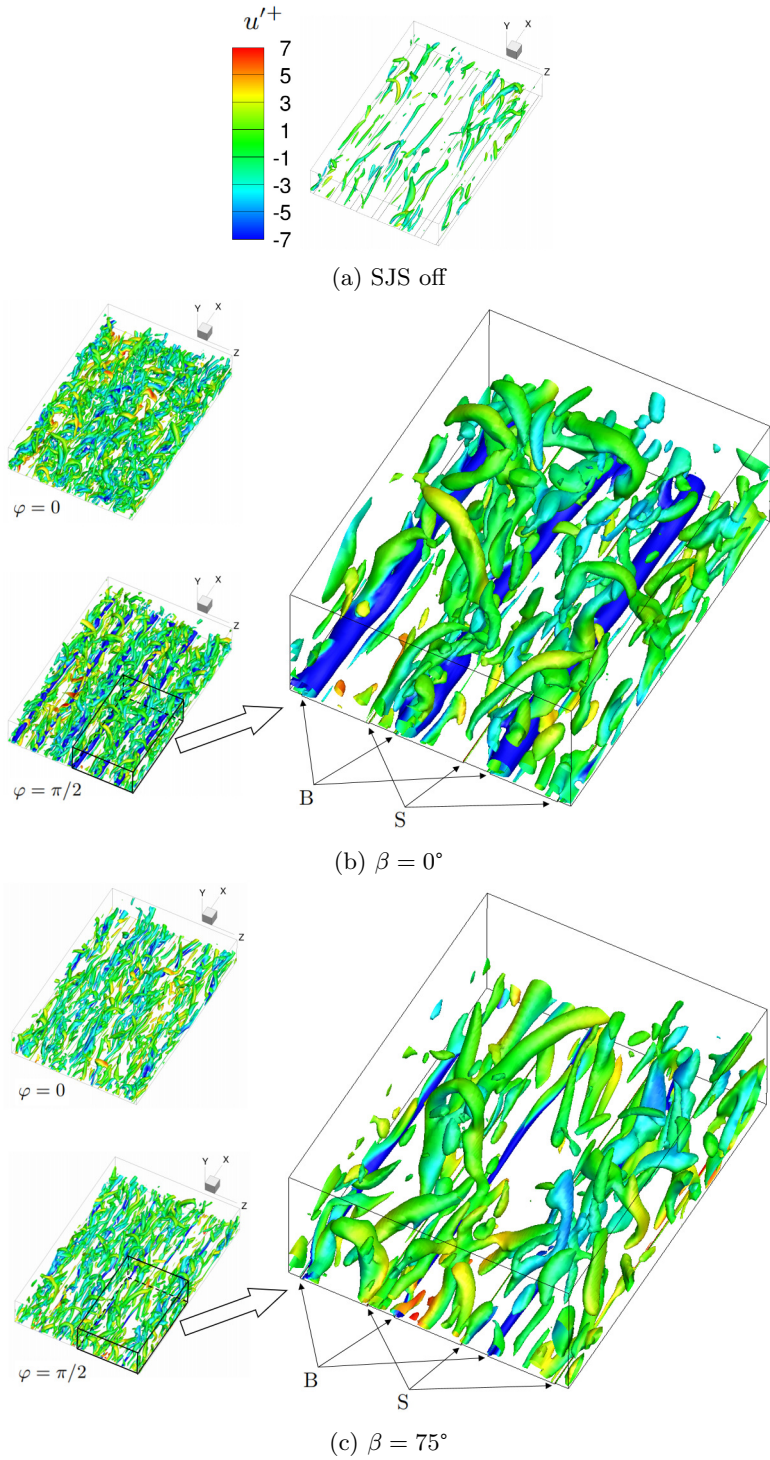
Figure 11: Isosurfaces of $\lambda_2^+ = -2$ at different phases for the cases with SJS off, $\beta = 0°$, and 75°. The isosurfaces are coloured by u'^+. 'B' and 'S' stand for blowing and suctioning slots, respectively.
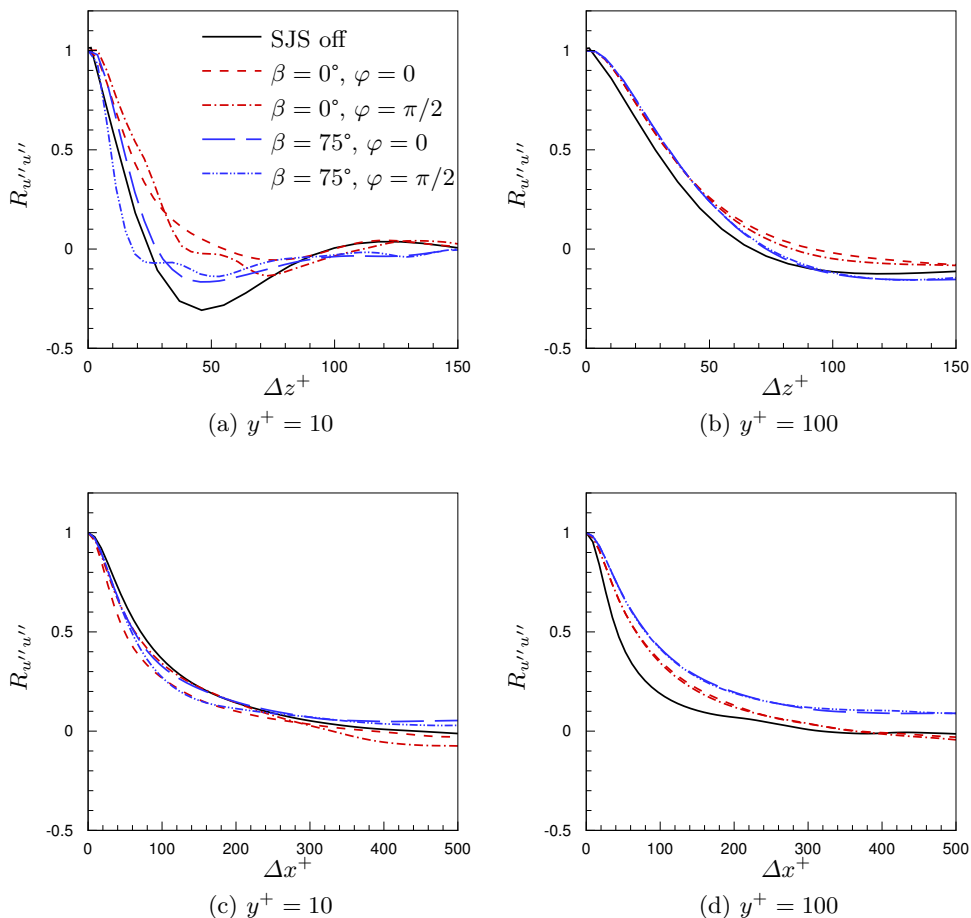
Figure 12: Spanwise and streamwise two-point correlations of streamwise velocity fluctuations, u''.

structures, shaped like elongated tubes near the SJS slots, are generated during blowing, at the phase $\varphi = \pi/2$. At the phase $\varphi = 0$ and during suction, the vortical structures are broken by the main flow and the vortices are more apart than when $\varphi = \pi/2$. Figure 11 shows that the diameter and the intensity of the weaker vortices, coloured in green and located in the bulk of the flow, are only slightly influenced by the SJS angle. In the $\beta = 0°$ case, intense elongated tubular structures appear near the wall and in the proximity of the SJS exits where blowing occurs. These structures are much weaker in the $\beta = 75°$ case.

Two-point autocorrelations, defined as

$$R_{u''u''}(\Delta x_i) = \frac{\overline{u''(x_i + \Delta x_i)u''(x_i)}}{\overline{u''u''}}, \tag{3.1}$$

are computed for $x_i = x, z$. Figure 12 shows the distributions of $R_{u''u''}(\Delta x)$ and $R_{u''u''}(\Delta z)$ at different heights for cases with SJS off, $\beta = 0°$ and $\beta = 75°$. Figure 12(a) shows that at $y^+ = 10$, for $\beta = 75°$, the spanwise turbulent length scales are smallest, while, for $\beta = 0°$, the scales are largest, confirming quantitatively what observed in the
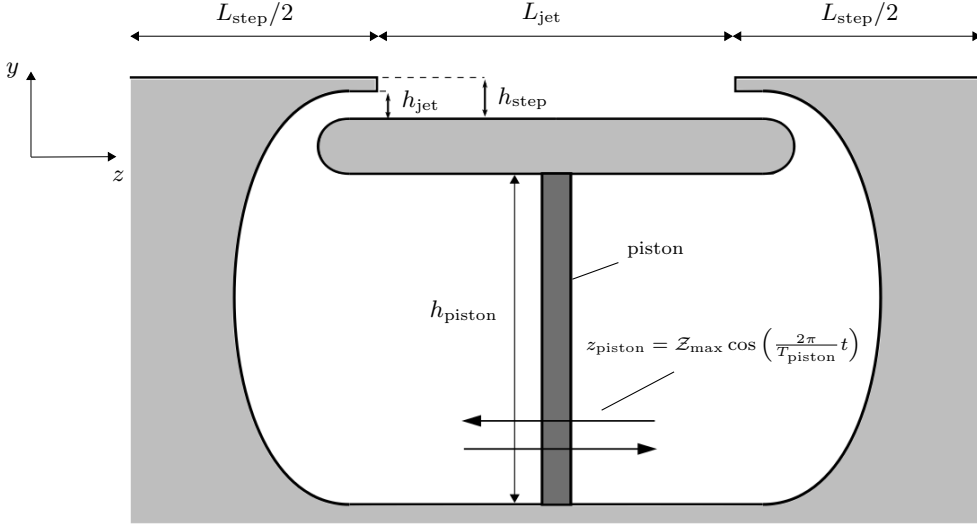
Figure 13: Schematic of the cavity chambers. The thickness of the piston is not to scale.

flow visualizations of figure 11. In figure 12(b), the $R_{u''u''}(\Delta z^+)$ values at higher locations ($y^+ = 100$) are similar for both SJS cases, as also shown by the green vortices in figure 11. Figure 12(c) shows that, at $y^+ = 10$, the streamwise turbulent length scales are reduced slightly by SJS, and the case $\beta = 0°$ shows the shortest scales when the SJS velocity amplitude reaches its maximum. Figure 12(d) shows that, at $y^+ = 100$, the SJS increase the length scales the most when $\beta = 75°$. The SJS influence the spanwise length scales more than the streamwise length scales.

3.4. Flow and power balance of the jet-sheet actuator

A model of the actuators that generate the SJS is presented in this section. The focus is on the flow inside the actuators, located underneath the channel walls, and on the power required to operate the SJS. As for the turbulent channel flow simulations, the channel half-height h^* and the centreline velocity U_p^* of the laminar parabolic Poiseuille flow of the reference smooth channel case are used for scaling.

3.4.1. Flow in the cavity chambers

Figure 13 shows a schematic of the system. A piston separates two chambers of a cavity and oscillates sinusoidally along the spanwise direction, forcing the fluid in the compression chamber to discharge through the SJS opening and out into the channel. Simultaneously, the pressure drops in the suction chamber, causing the fluid to enter the SJS opening and to fill the chamber. The flows in the chambers alternate their behaviour every half cycle, according to the motion of the piston. The parameters of the chambers and the simulation details are listed in table 2.

The in-house code SHEFFlow is used to compute the flow in the chambers and outside of the SJS openings. The domain of the simulation consists of the chambers and half of the channel above them. The flow is assumed to be two-dimensional. Mirror boundary conditions are imposed at the half channel boundary and periodic boundary conditions are enforced at the sides of the computational domain. Figure 13 represents the purely spanwise case ($\beta = 0°$). In the case of oblique SJS, the exits would require inclined vanes to drive the fluid out into the channel at an angle. The losses due to the three-dimensionality

L_{step}	L_{jet}	h_{piston}	h_{jet}	h_{step}	$\langle w \rangle_{\mathrm{jet,max}}$	T_{piston}	Δt	U_p^* (m/s)
0.2	0.5	0.278	0.0111	0.0139	0.7714	16.2	$3.24 \cdot 10^{-3}$	63

Table 2: Simulation and chamber parameters. $\langle w \rangle_{\mathrm{jet,max}}$ is the spatially averaged SJS velocity and Δt is the time step. The other quantities are defined in figure 13.

of the vanes are assumed small with respect to the rest of the losses, an approximation that is confirmed in §3.4.4. The wall that separates the SJS and the channel has a finite thickness, which is smaller than the height of the exits. This finite thickness avoids a sharp wall end at the exit, which would create intense velocity gradients when the fluid leaves the chamber.

Figure 14 shows that the density and the temperature are not uniform inside the chambers. When the piston is in the neutral position ($\varphi = \pi/2$), the piston velocity is maximum. The fluid is then compressed in the right chamber, while in the left chamber the fluid expands. At $\varphi = 0$, the displacement is maximum and the density in the right chamber decreases by releasing the fluid inside the chamber to the channel, while, in the left chamber, the fluid enters the chamber and the density increases. These compressibility effects cause a phase lag of about $\varphi = 0.03\pi$ between the pressure experienced by the piston and the velocity of the piston, rendering the power spent lower than that without delay.

Figure 15 shows that the computed horizontal SJS velocity profiles are approximated well by parabolic profiles. The results of the two-dimensional simulation therefore validate the assumption of a parabolic SJS flow for the three-dimensional channel-flow simulation, modelled by equation (2.4). The largest deviations from a symmetric profile occur when the mass flow rate is maximum during blowing or suction. When air exits a chamber and enters the channel, the peak of the maximum velocity is slightly larger than in the mid position at $y^+ = 1$, while the contrary happens in the suction phase, during which the maximum velocity peak is lower than in the mid position. In the blowing phase, this small effect is caused by a localized region of low pressure at the tip of the step wall. This low pressure causes the air exiting the SJS aperture to move upward, away from the jet wall. In the suction phase, the curvature of the chamber forces the air in the lower half of the SJS aperture to turn downwards.

3.4.2. *Motion of the piston*

The position of the piston is described by

$$z_{\mathrm{piston}} = \mathscr{Z}_{\mathrm{max}} \cos\left(\frac{2\pi}{T_{\mathrm{piston}}}t\right), \tag{3.2}$$

where T_{piston} is the period of oscillation of the piston and $\mathscr{Z}_{\mathrm{max}}$ is the maximum displacement travelled by the piston with respect to the central position. The period of oscillation T_{piston} is the same as the period of oscillation T_{osc} of the SJS boundary condition in the full three-dimensional simulation.

As the flow inside the chambers is compressible, an exact a priori relationship between the piston motion and the SJS velocity cannot be found without simulating the flow because the fluid density at the piston surfaces and the fluid density at the cavity exits are not known. Therefore, in order to obtain an estimate of the maximum displacement
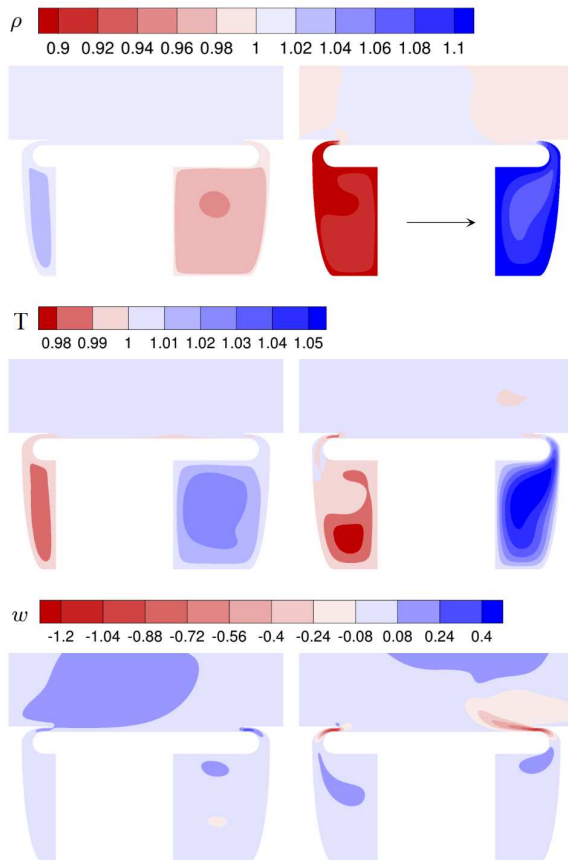
Figure 14: Contours of the density (top), temperature (middle) and spanwise velocity (bottom) at phases $\varphi = 0$ (left) and $\varphi = \pi/2$ (right). The horizontal arrow indicates the direction of piston motion.
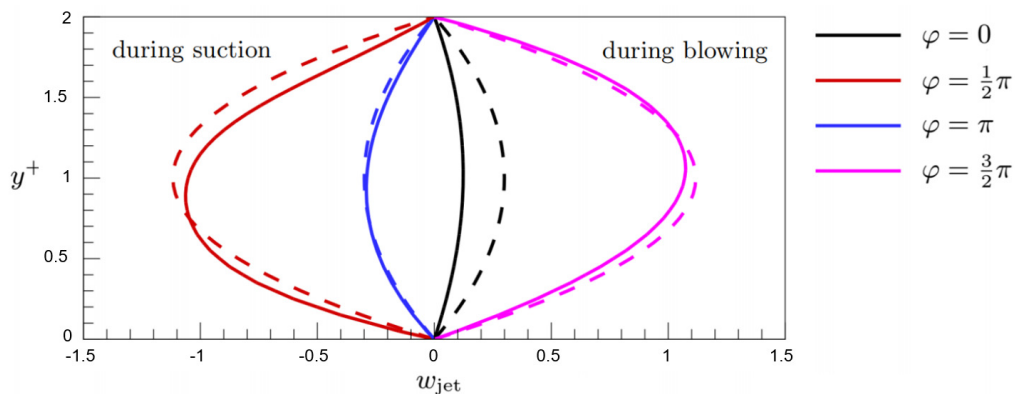
Figure 15: Velocity profiles at the exit of the left cavity at different phases of the oscillation. The dashed lines represent the parabolic boundary condition given in (2.4), imposed in the three-dimensional channel flow simulations. The solid lines represent the velocity profiles obtained with the 2D simulation.

$\mathcal{Z}_{\mathrm{max}}$ as a function of the average SJS velocity, the incompressible mass conservation equation is used,

$$\int_A \mathbf{u} \cdot \mathbf{n} \mathrm{d}A = 0, \tag{3.3}$$

where A is the surface of the chamber including the SJS orifices and $\mathbf{n}$ is the normal unit vector perpendicular to A, pointing outwards. Since the vectors $\mathbf{n}$ for the piston surface and for the SJS exit surface point in the spanwise direction, (3.3) becomes

$$-w_{\mathrm{piston}}(t) A_{\mathrm{piston}} + \int_{A_{\mathrm{fluid}}} w_{\mathrm{jet}}(y, t) \mathrm{d}A_{\mathrm{fluid}} = 0, \tag{3.4}$$

where w_{piston} is the velocity of the piston, w_{jet} is the velocity profile at the SJS exit, A_{piston} is the surface of the piston and A_{fluid} is the area of the SJS apertures. Writing (3.4) per unit depth, the surface integral becomes

$$-w_{\mathrm{piston}}(t) h_{\mathrm{piston}} + \int_0^{h_{\mathrm{jet}}} w_{\mathrm{jet}}(y, t) \mathrm{d}y = 0, \tag{3.5}$$

where h_{piston} is the height of the piston. The spatial mean velocity of the SJS, defined as

$$\langle w \rangle_{\mathrm{jet}}(t) = \frac{1}{h_{\mathrm{jet}}} \int_{h_{\mathrm{jet}}} w_{\mathrm{jet}}(y, t) \mathrm{d}y, \tag{3.6}$$

and w_{piston}, found from differentiating (3.2), are substituted into (3.5) to find the maximum displacement of the piston,

$$\mathcal{Z}_{\mathrm{max}} = \frac{T_{\mathrm{piston}}}{2\pi} \frac{h_{\mathrm{jet}}}{h_{\mathrm{piston}}} \langle W \rangle_{\mathrm{jet,max}}, \tag{3.7}$$

where $\langle W \rangle_{\mathrm{jet,max}}$ is the maximum spatial mean velocity of the SJS within a period. The boundary conditions for the SJS velocity in the three-dimensional simulation with the parameters given in table 2 result in an amplitude of $\mathcal{Z}_{\mathrm{max}} = 0.079$ and a maximum piston velocity of $W_{\mathrm{piston,max}} = 0.031$.

3.4.3. *Power balance of the cavity flow for $\beta = 0°$*

The first step to study the power balance of the SJS actuators is to calculate the power per unit depth required to move the piston, $\mathcal{W}_{\mathrm{piston}}$, in the two-dimensional configuration ($\beta = 0°$). This power is exerted by the force that the piston has to overcome at any time to generate the SJS, given by the difference of the integrated pressures on the two sides of the piston as a function of time. The power $\mathcal{W}_{\mathrm{piston}}$ is

$$\mathcal{W}_{\mathrm{piston}}(t) = w_{\mathrm{piston}}(t) \int_{h_{\mathrm{piston}}} \Delta p_{\mathrm{piston}}(y, t) \mathrm{d}y, \tag{3.8}$$

where $\Delta p_{\mathrm{piston}}$ is the difference of the pressure on the two sides of the piston. Figure 16 shows the piston velocity $w_{\mathrm{piston}}(t)$, the force per unit depth of the cavity acting on the piston,

$$F_{\mathrm{piston}}(t) = \int_{h_{\mathrm{piston}}} \Delta p_{\mathrm{piston}}(y, t) \mathrm{d}y, \tag{3.9}$$

and the power $\mathcal{W}_{\mathrm{piston}}$ during a period of oscillation. A phase lag of about $\varphi = 0.1\pi$, shown in figure 16, occurs between the integrated pressure $\Delta F_{\mathrm{piston}}$ experienced by the
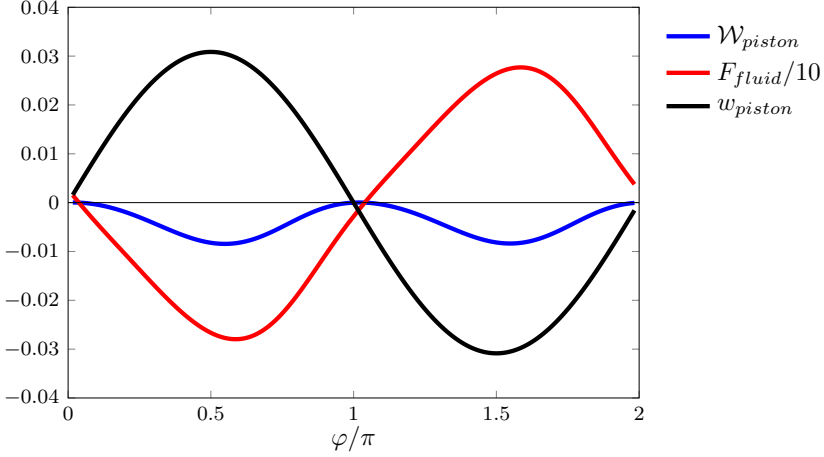
Figure 16: Ensemble average of the velocity of the piston, pressure difference, and power required to move the piston.

piston and the velocity of the piston $w_{\text{piston}}(t)$. This phase lag causes the power spent to be lower than that if the maxima of the piston force and the piston velocity occurred at the same time. For the parameters given in table 2, the average power required to move the piston is $\overline{\mathcal{W}}_{\text{piston}} = 8 \cdot 10^{-3}$.

The power balance inside the cavity chambers is studied through the balance equation for the total power integrated over the control volume. The balance equation, derived in Appendix C following Panton (2013), reads

$$
\underbrace{\frac{\mathrm{d}}{\mathrm{d}t} \int_V \rho \left(e + \frac{|\mathbf{u}|^2}{2} \right) \mathrm{d}V}_{\mathrm{d}\mathcal{E}/\mathrm{d}t} = - \underbrace{\int_{A_{fluid}} p\mathbf{u} \cdot \mathbf{n} \mathrm{d}A}_{\mathcal{P}_{fluid}} - \underbrace{\int_{A_{fluid}} \rho e \mathbf{u} \cdot \mathbf{n} \mathrm{d}A}_{\mathcal{F}_{i-fluid}} -
$$

$$
\underbrace{\int_{A_{fluid}} \rho \frac{|\mathbf{u}|^2}{2} \mathbf{u} \cdot \mathbf{n} \mathrm{d}A}_{\mathcal{F}_{m-fluid}} - \underbrace{w_{\text{piston}}(t) \int_{A_{piston}} \Delta p_{\text{piston}} \mathrm{d}A}_{\mathcal{W}_{\text{piston}}} + \underbrace{\frac{1}{Re_p} \int_{A_{fluid}} (\boldsymbol{\tau} \cdot \mathbf{u}) \cdot \mathbf{n} \mathrm{d}A}_{\mathcal{T}_{fluid}} +
$$

$$
\underbrace{\frac{1}{Re_p} \int_A k \nabla \mathrm{T} \cdot \mathbf{n} \mathrm{d}A}_{\mathcal{Q}}. \tag{3.10}
$$

Equation (3.10) expresses the following physical mechanisms. The power injected into the cavity chambers via the pressure work of the piston $\mathcal{W}_{\text{piston}}$ partly generates the time rate of change of the integrated total energy, $\mathrm{d}\mathcal{E}/\mathrm{d}t$, is partly transferred to the channel as the fluid exhausts through the SJS apertures, via the flux of internal energy per unit time $\mathcal{F}_{i-fluid}$, the mechanical-power flux $\mathcal{F}_{m-fluid}$, the pressure work $\mathcal{P}_{fluid}$ and the shear-stress work $\mathcal{T}_{fluid}$ of the SJS, and is lost to the outside of the cavity chambers via the heat transfer $\mathcal{Q}$.

Figure 17 shows the time evolution of the terms of equation (3.10) during one period of oscillation. The kinetic energy term $\mathrm{d}\mathcal{E}/\mathrm{d}t$ shows the most intense oscillations, while the power transferred via the shear stresses at the SJS apertures, $\mathcal{T}_{fluid}$, is found to be negligible. At any phase of the oscillation, the piston always injects power into the chambers, while heat is always extracted from the chambers. The flux terms and the
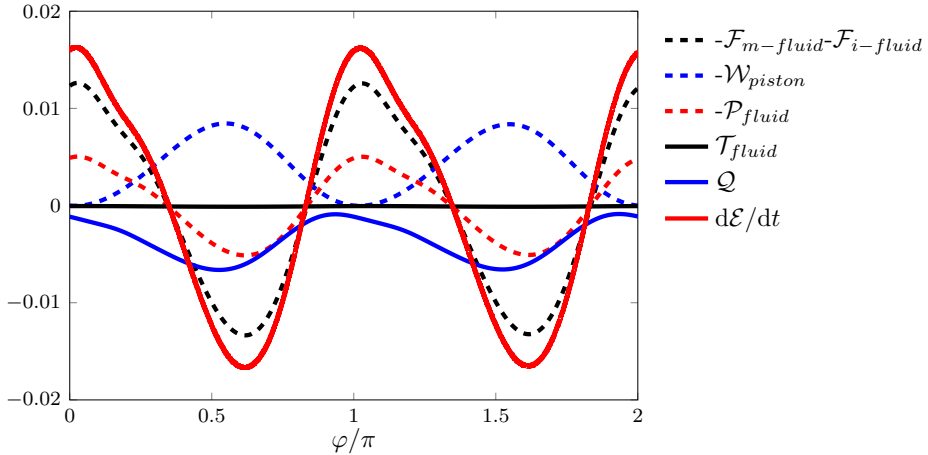
Figure 17: Time evolution of terms in the power equation (3.10). Positive values indicate power into the chambers, while negative values indicate power lost from the chambers.
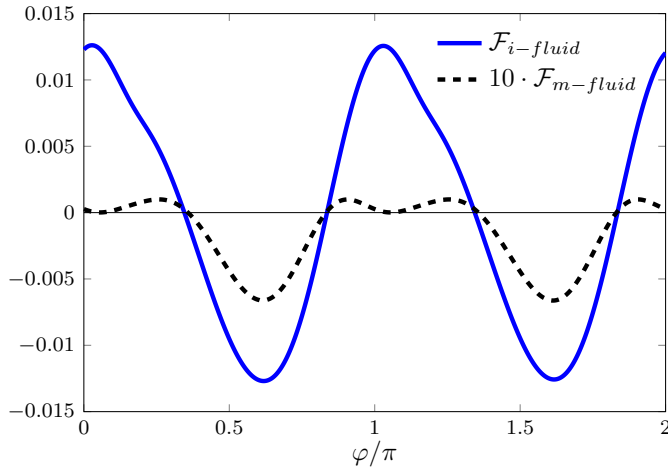

Figure 18: Time evolution of mechanical-power flux $\mathcal{F}_{m-fluid}$ and the flux of internal energy per unit time $\mathcal{F}_{i-fluid}$.

pressure term related to the SJS instead oscillate between positive and negative values, being directly related to the SJS.

Figure 18 displays the time evolution of the flux terms $\mathcal{F}_{m-fluid}$ and $\mathcal{F}_{i-fluid}$. The flux of internal energy per unit time $\mathcal{F}_{i-fluid}$ is much larger than the mechanical-power flux $\mathcal{F}_{m-fluid}$ because the difference in temperature at the SJS exits is larger than the difference in the averaged velocities. Mechanical power is passed from the chambers to the channel for 47% of an oscillating period, during $(0.31\pi, 0.86\pi)$ and $(1.31\pi, 1.86\pi)$. The time-averaged values of the fluxes of mechanical power and internal energy per unit time are $3.04 \cdot 10^{-4}$ and $1.84 \cdot 10^{-4}$, i.e., the mechanical part takes 62.3% of the convective flux and is 3.8% of the time average of $\mathcal{W}_{\text{piston}}$.

The terms in equation (3.10) are time averaged to further quantify the balance of the SJS actuator. The averaged values are listed in table 3. For the convective flux and the pressure work, power flows into the two chambers when the value is negative and out

$$\left| \begin{array}{c} \overline{\mathcal{F}}_{m-fluid} + \overline{\mathcal{F}}_{i-fluid} \\ 0.49 \cdot 10^{-3} \end{array} \right| \begin{array}{c} \overline{\mathcal{Q}} \\ -7.29 \cdot 10^{-3} \end{array} \left| \begin{array}{c} \overline{\mathcal{W}}_{piston} \\ -8.04 \cdot 10^{-3} \end{array} \right| \begin{array}{c} \overline{\mathcal{P}}_{fluid} \\ 0.14 \cdot 10^{-3} \end{array} \left| \begin{array}{c} \overline{\mathcal{T}}_{fluid} \\ -0.12 \cdot 10^{-3} \end{array} \right|$$

Table 3: Time-averaged terms in equation (3.10).

of them when the value is positive. The channel flow thus receives power from the SJS in the three ways, i.e., through the flux of internal energy per unit time $\overline{\mathcal{F}}_{i-fluid}$, the mechanical-power flux $\overline{\mathcal{F}}_{m-fluid}$, and the pressure-work term $\overline{\mathcal{P}}_{fluid}$. The last two types of power are relevant for flow control: $\overline{\mathcal{F}}_{m-fluid}$ and $\overline{\mathcal{P}}_{fluid}$ are 3.8% and 1.7% of $\overline{\mathcal{W}}_{\text{piston}}$, respectively. The effective power $\overline{\mathcal{P}}_{\text{jet-sheet}}$ is

$$\overline{\mathcal{P}}_{\text{jet-sheet}} = \overline{\mathcal{F}}_{m-fluid} + \overline{\mathcal{P}}_{fluid} = 0.038 \cdot \overline{\mathcal{W}}_{\text{piston}} + 0.017 \cdot \overline{\mathcal{W}}_{\text{piston}} = 0.054 \cdot \overline{\mathcal{W}}_{\text{piston}}. \tag{3.11}$$

The efficiency of the SJS actuator is therefore $\overline{\mathcal{P}}_{\text{jet-sheet}}/\overline{\mathcal{W}}_{\text{piston}} = 5.4\%$. A more conservative estimation of the power employed by distributed suction and blowing was utilized by Bewley *et al.* (2001), Chung & Talha (2011), and Stroh *et al.* (2015). They used the absolute values of the integrands that define $\overline{\mathcal{F}}_{m-fluid}$ and $\overline{\mathcal{P}}_{fluid}$, as defined in equations (3.12) and (3.13). If we adopt those authors' definitions of power consumption,

$$|\overline{\mathcal{F}}_{m-fluid}| = \int_{T_{\text{osc}}} \int_{A_{fluid}} |\rho \frac{|\mathbf{u}|^2}{2} \mathbf{u} \cdot \mathbf{n}| \mathrm{d}A \mathrm{d}t, \tag{3.12}$$

$$|\overline{\mathcal{P}}_{fluid}| = \int_{T_{\text{osc}}} \int_{A_{fluid}} |p\mathbf{u} \cdot \mathbf{n}| \mathrm{d}A \mathrm{d}t, \tag{3.13}$$

we find $|\overline{\mathcal{F}}_{m-fluid}| = 0.42 \cdot 10^{-3} = 0.052 \cdot \overline{\mathcal{W}}_{\text{piston}}$ and $|\overline{\mathcal{P}}_{fluid}| = 6.22 \cdot 10^{-3} = 0.774 \cdot \overline{\mathcal{W}}_{\text{piston}}$.

3.4.4. *Power balance of the cavity flow for* $\beta \neq 0°$

The analysis of the power efficiency of the cavity flow presented in §3.4.3 is limited to the two-dimensional case with injection angle $\beta = 0°$. To compute the power efficiency of the cavity flow for finite angles β, we estimate the power loss by considering the flow through a series of guide vanes placed between the cavity and the SJS exits, as shown in figure 19. For the power-loss estimation, it is useful to refer to studies on flows through guide vanes in low-speed wind tunnels. The Reynolds number Re_c used in the analysis of guide vanes is typically based on the mean inlet velocity and the chord of the guide vanes; in our case, a sound estimate based on the maximum inlet velocity is $Re_c = 25000$. According to Sahlin & Johansson (1991) and Lindgren *et al.* (1998), the guide-vane pressure loss coefficient $\mathcal{K}$ at this chord Reynolds number for a 90° turn and expansion ratios close to unity varies in the range

$$\mathcal{K} = \frac{\Delta H^*}{q_{\text{in}}^*} = 0.08 - 0.12, \tag{3.14}$$

where $\Delta H^* = (p_{\text{in}}^* + q_{\text{in}}^*) - (p_{\text{out}}^* + q_{\text{out}}^*)$, the subscripts "in" and "out" stand for the flow entering and exhausting from the vane, respectively, and $q_{\text{in}}^* = \rho_c^* \langle W \rangle_{\text{jet,max}}^{*2} /2 = q_{\text{out}}^*$ because the expansion ratio is assumed to be unity. A 90° turning vane represents the worst possible scenario for the power loss and adequately models the SJS case with
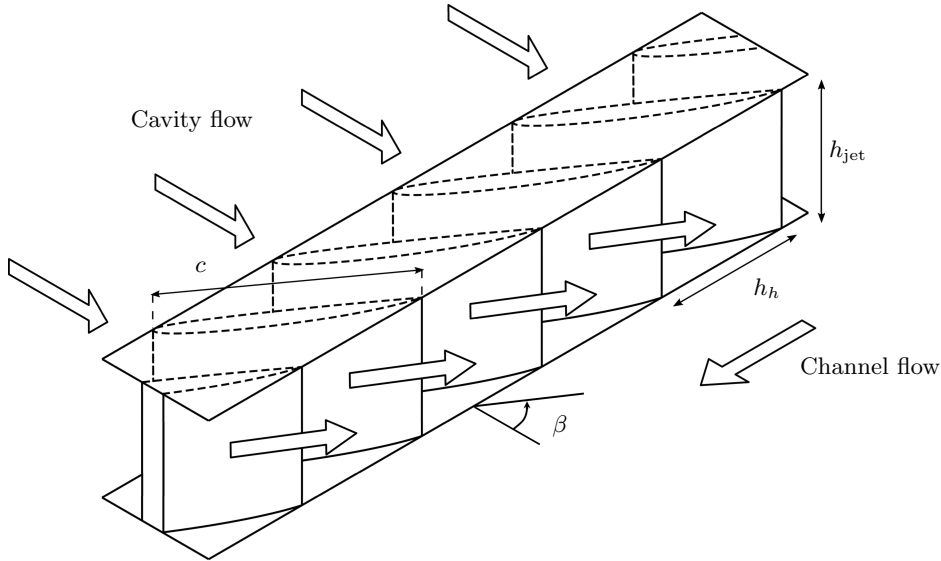
Figure 19: Schematic of the guide vanes used to change the direction of the flow to an angle β.

$\beta = 75°$, which leads to the maximum drag reduction. The estimate of the pressure coefficient translates to a 10% decrease of the mechanical-power flux, $\overline{\mathcal{F}}_{m-fluid}$, injected into the channel. The overall efficiency of the device reduces to 5.2%. Moreover, it means that the case with $\beta = 75°$ needs $1.11 \cdot \overline{\mathcal{W}}_{\text{piston}}$ to have the same amount of power at the SJS exits as the case with $\beta = 0°$.

It is also instructive to compare the power used to activate the piston with the power saved by drag reduction. From equation (2.13), the power spent per streamwise length used to drive the fluid in the channel is

$$\overline{\mathcal{P}}^*_{\text{channel}} = 2\tau_w^* U_b^* (L_{\text{jet}}^* + L_{\text{step}}^*) = [C_f]\rho_c^* U_b^{*3}(L_{\text{jet}}^* + L_{\text{step}}^*). \qquad (3.15)$$

Using the channel half-height h^* and the centreline velocity U_p^* for scaling, one finds

$$\overline{\mathcal{P}}_{\text{channel}} = [C_f] \left(\frac{U_b^*}{U_p^*}\right)^3 \frac{L_{\text{jet}}^* + L_{\text{step}}^*}{h^*} = 16.97 \cdot 10^{-4}. \qquad (3.16)$$

For $\beta = 75°$, the skin-friction coefficient is reduced by 10.5%, which leads to the maximum power saved by the SJS actuation, $\overline{\mathcal{P}}_{\text{channel,SJSoff}} - \overline{\mathcal{P}}_{\text{channel,SJS75}} = 17.82 \cdot 10^{-5}$. The net power saved in this case is $\overline{\mathcal{P}}_{\text{channel,SJSoff}} - \overline{\mathcal{P}}_{\text{channel,SJS75}} - 1.11 \cdot \overline{\mathcal{W}}_{\text{piston}} = -8.75 \cdot 10^{-3}$, which means that the actuation power is larger than the saved power due to drag reduction.

4. Conclusions

Skin-friction drag reduction generated by wall-tangential synthetic jet sheets in a turbulent channel flow at $Re_\tau = 180$ has been investigated by direct numerical simulations. The jet sheets eject from slots located below steps that are aligned along the streamwise direction. The effect of the jet-sheet angle with respect to the streamwise direction has been studied. Compared to the smooth channel flow, the friction drag decreases by 10.5%

and increases by 98.4% for thin jet heights of $h_{\mathrm{jet}}^+ = 2$ and jet-sheet angles equal to 75° and 0°, respectively. Drag reduction margins as large as 30% are obtained for jet sheets exhausting from thicker slots and for distances between slots smaller than the spanwise length scale of the low-speed streaks. The drag reduction on the jet walls offsets the drag increase on the step walls for a jet-sheet angle $\beta = 75$°. The spatially averaged skin-friction coefficients fluctuates in time with a period that is half of the jet-sheet period.

In all the cases, there occurs an intense variation of the wall-shear stress along the spanwise direction. The phase averaged results indicate that blowing decreases the drag and suction increases it. When the jet sheets eject at a large angle, the time and spatially averaged results show that the friction drag decreases significantly near the slots. Although the jet sheets are synthetic and therefore their net mass flow rate is null, the global friction drag reduction is caused by a net negative wall-shear stress near the jet-sheet openings, which is due to the nonlinear interaction between the jet sheets and the streamwise mean flow.

The velocity fluctuations and the Reynolds stresses in the controlled cases are larger than those for the cases with jet sheets off. The total fluctuations are enhanced because the jet sheets add periodic perturbation into the flow and because the purely turbulent fluctuations are also enhanced. The growth of velocity fluctuations causes the total and purely turbulent Reynolds shear stresses to increase with respect to the reference case when the jet sheets are on, even when drag reduction occurs. Instantaneous flow visualizations also show that eddies are more intense when the flow is forced by the jet sheets. Low-speed and high-speed regions are elongated by the jet sheets when the jet-sheet velocity increases. For $\beta = 0$°, the vortices are closer to the channel centre than for $\beta = 75$°. For $\beta = 0$°, the spanwise length scales of the vortices are wider than those for $\beta = 75$°, as shown by two-point autocorrelations.

A power balance analysis has also been carried out for the actuator by simulating the flow inside a cavity where a piston creates the air motion that generates the jet sheets. As air is cyclically compressed or expanded inside the chambers, the power input by the piston is transferred to the jet sheets, but also transformed into internal energy per unit time and lost via heat transfer instead of being used as kinetic energy of the jet sheets. During part of the cycle, the compressed air expands, transforming internal energy into kinetic energy. For the tested configurations, the power spent to generate the jet sheets is larger than that saved thanks to the reduction of wall friction. It would be interesting to test the actuator with a fluid that does not experience the compressibility effects of air, like water, in order to improve the power efficiency of the actuator.

It would also be of interest to investigate the flow at larger Reynolds numbers or when driven by a constant pressure gradient. Future research should be directed to discerning how the periodic jet-sheet flow interacts with the bulk turbulent flow to generate the counter flow, a mechanism recognized to be responsible for the drag-reduction effect. In view of technological applications, it would be relevant to study the persistence of the turbulent-flow modifications downstream of a finite section of the wall surfaces where the jet sheets are enforced.

Acknowledgements

Cases	L_x	L_z	$[C_f] \cdot 10^3$	$\mathcal{E}(\%)$	Mesh size
1	4π	$4\pi/3$	8.16	-0.24	$64 \times 128 \times 84$
2	4π	$10\pi/9$	8.19	0.12	$64 \times 128 \times 70$
3	4π	$8\pi/9$	8.20	0.24	$64 \times 128 \times 56$
4	3π	$4\pi/3$	8.19	0.12	$48 \times 128 \times 84$
5	3π	$10\pi/9$	8.20	0.24	$48 \times 128 \times 70$
6	3π	$8\pi/9$	8.20	0.24	$48 \times 128 \times 56$
7	2π	$4\pi/3$	8.17	-0.12	$32 \times 128 \times 84$
8	2π	$10\pi/9$	8.15	-0.37	$32 \times 128 \times 70$
9	2π	$8\pi/9$	8.10	-0.98	$32 \times 128 \times 56$

Table 4: Skin-friction coefficients and errors for different sizes of computational domain, using the same mesh resolution. $\Delta x^+ = 17.67$, $\Delta z^+ = 8.98$, $\Delta y_w^+ = 0.5$, $\Delta y_c^+ = 5.56$. $\mathcal{E} = 100 \cdot ([C_f] \cdot 10^3 - 8.18)/8.18$.

studies. The authors acknowledge the provision of computing resources on the High Performance Computing cluster ShARC at the University of Sheffield and the Sunway TaihuLight at the National Supercomputing Center in Wuxi, China.

Declaration of interests

The authors report no conflict of interest.

Appendix A. Validation of the numerical computations

The computation of the fully developed turbulent channel flow at $Re_\tau = 180$ is validated by several resolution checks. Table 4 shows the results of mesh independence. For case 1, the dimensions of the computational domain are $L_x = 4\pi$ and $L_z = 4\pi/3$ for the streamwise length and spanwise width, respectively. The reference mesh resolutions are $\Delta x^+ = 17.67$ and $\Delta z^+ = 8.98$ in the streamwise and spanwise directions, respectively, while $\Delta y_w^+ = 0.5$ is the distance of the first wall-normal grid point from the walls and $\Delta y_c^+ = 5.56$ is the wall-normal grid spacing at the channel centre. The reference mesh has $128 \times 128 \times 84$ cells in the streamwise, wall-normal and spanwise directions, respectively.

After the flow has reached its fully developed turbulent state, the skin-friction coefficient is computed to be $[C_f] = 8.16 \cdot 10^{-3}$ by averaging flow fields between $t^+ = 2187$ and $t^+ = 4860$. This value is only 0.24% different from the $[C_f] = 8.18 \cdot 10^{-3}$ from the DNS simulation by Kim *et al.* (1987). The mean streamwise velocity, the root-mean-square of the velocity fluctuations, the Reynolds shear stresses, and the streamwise spectra of velocities are undistinguishable from the corresponding quantities reported by Kim *et al.* (1987), as shown in figure 20. Case 7 is chosen as a compromise between a manageable computational cost and accuracy of the computation of the skin-friction coefficient. The comparisons of the mesh resolutions and the results are shown in table 5 for the smooth channel.

The mesh sensitivity was also studied for the controlled channel. Since the cases of 75° and $\beta = 0°$ have large values of drag reduction and drag increase, they are chosen for the validation tests. The baseline mesh is similar to the resolution of the medium mesh. Figure 21 displays how the mesh is refined in the spanwise direction. Table 6 shows the skin-friction coefficients for different mesh resolutions. To study the mesh sensitivity,
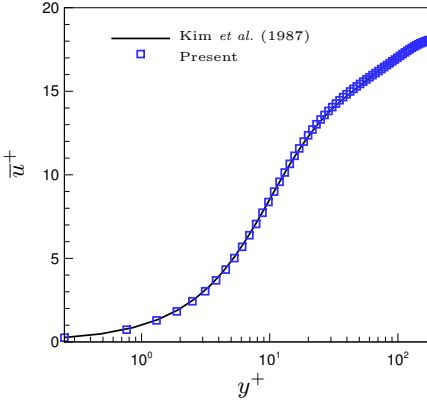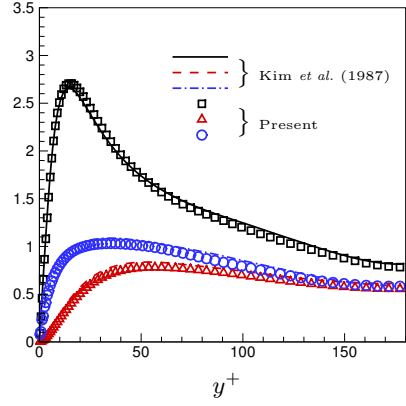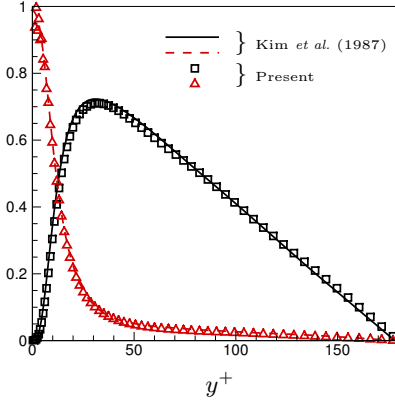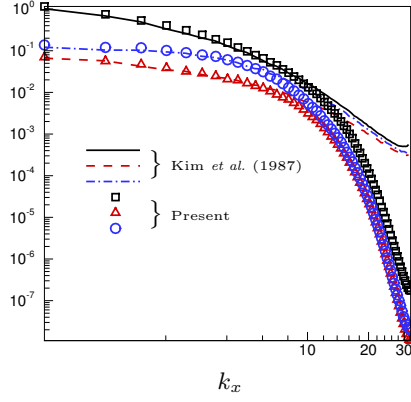
(a) Mean streamwise velocity profile.

(b) Root-mean-square of velocity fluctuations: u'^+_{rms}, ——, □; v'^+_{rms}, − − −, △; w'^+_{rms}, −·−·−, ○.

(c) Comparisons of the normalized viscous shear stress $\mu\frac{\partial \overline{u}}{\partial y}/\tau_w$, − − −, △; and Reynolds shear stress $-\overline{u'v'}/\tau_w$, ——, □.

(d) Streamwise spectra for u, v, w at $y^+ = 30$ with E_{uu}, ——, □; E_{vv}, − − −, △; E_{ww}, −·−·−, ○.

Figure 20: Comparisons of the flow quantities of Kim *et al.* (1987) and SHEFFlow.

Cases	Δx^+	Δz^+	Δy^+_w	Δy^+_c	$\mathcal{E}(\%)$	Mesh size
Coarse	17.67	8.98	0.5	5.56	-0.12	$64 \times 128 \times 84$
Medium	8.84	4.49	0.2	4.13	0.24	$128 \times 197 \times 168$

Table 5: Skin-friction coefficients and errors for different mesh resolutions.

the baseline mesh is refined in three directions. Cases A, B and C are refined in the streamwise, wall-normal and spanwise directions, respectively. Comparing the results of the baseline case and case A, the differences of the skin-friction coefficients are 0.12% and 0.43% for $\beta = 0°$ and $\beta = 75°$, respectively. The differences between the baseline case

(a) Baseline (b) C1
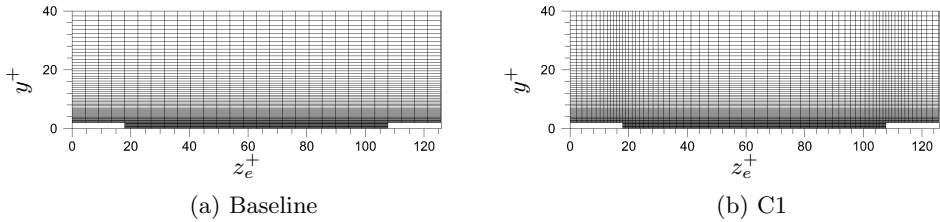
Figure 21: Computational meshes for the study of mesh sensitivity.

Cases	Δx^+	$\Delta z^+_{\min}$	$\Delta z^+_{\max}$	Δy^+_w	Δy^+_c	Mesh size	$[C_{f,0°}] \cdot 10^3$	$[C_{f,75°}] \cdot 10^3$
Baseline	8.84	4.49	4.49	0.2	4.09	$128 \times 197 \times 168$	16.46	6.92
A	4.42	4.49	4.49	0.2	4.09	$256 \times 197 \times 168$	16.44	6.89
B	8.84	4.49	4.49	0.1	4.06	$128 \times 297 \times 168$	16.48	6.88
C1	8.84	1.00	4.49	0.2	4.09	$128 \times 217 \times 396$	16.32	7.18
C2	8.84	0.50	3.80	0.2	4.09	$128 \times 217 \times 504$	16.23	7.32
C3	8.84	0.20	3.97	0.2	4.09	$128 \times 217 \times 648$	16.23	7.34

Table 6: Computational mesh resolutions and skin-friction coefficients for the study of mesh sensitivity at $\beta = 0°$ and $75°$.

and case B are 0.12% and 0.58% for $\beta = 0°$ and $\beta = 75°$, respectively. These differences are small, proving that the mesh values $\Delta x^+ = 8.84$, $\Delta y^+_w = 0.2$ and $\Delta y^+_c = 4.09$ are fine enough for computing the skin friction accurately. However, the results of the skin friction are very different between the baseline case and case C1, which means that the mesh resolution of the baseline case is not fine enough in the spanwise direction. As the mesh is refined in the spanwise direction, figure 22 shows a convergent trend of the skin frictions, the differences between cases C2 and C3 being negligible and 0.27% for $\beta = 0°$ and $\beta = 75°$, respectively. According to these results, the mesh resolution of case C2 is therefore fine enough to resolve the flow.
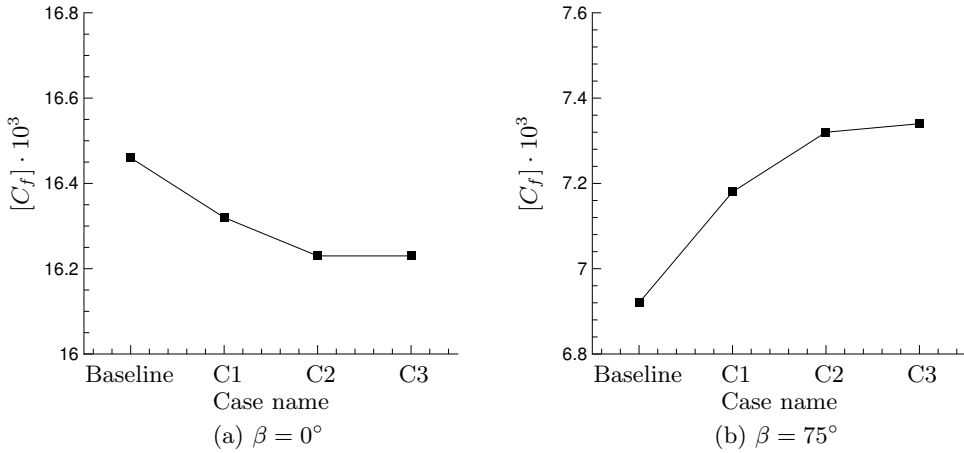
Figure 22: Skin-friction coefficients for the different meshes in Table 6.

Appendix B. Dependence of drag reduction on system parameters

The effects of the SJS slot height, velocity, period of oscillation, and length of the jet wall on the drag-reduction performance are investigated. As each parameter is varied independently, the other parameters are kept the same as the optimal case studied in the main text.

B.1. *Jet-sheet slot height*

For the uncontrolled cases, the results show that the skin-friction coefficients are $8.18 \cdot 10^{-3}$, $7.62 \cdot 10^{-3}$ and $7.54 \cdot 10^{-3}$ for $h_{\text{jet}}^+ = 2$, 4 and 8, respectively. The distributions of the time and spatially averaged skin-friction-coefficients along the spanwise direction are shown in figure 23. The effect of h_{jet}^+ is concentrated around the step corner, reducing the drag on the jet wall and increasing the drag on the step wall. The case of $h_{\text{jet}}^+ = 8$ produces the largest reduction in drag on the jet wall with respect to the smooth channel.

The drag-reduction margins for SJS slot heights $h_{\text{jet}}^+ = 2$, 4, 8 are shown in figure 24(a). Increasing the slot height enhances the drag-reduction effect and the largest drag reduction is achieved for $h_{\text{jet}}^+ = 8$ at a smaller optimal SJS angle than for $h_{\text{jet}}^+ = 2$, that is, $\mathcal{R}=26.8\%$ for $h_{\text{jet}}^+ = 8$ and $\beta = 45°$. Larger values of h_{jet}^+ imply larger mass flow rate for the SJS actuation, which leads to a more intense opposing streamwise component near the wall and thus larger drag reduction. Although $h_{\text{jet}}^+ = 4$ and 8 lead to larger drag-reduction margins than $h_{\text{jet}}^+ = 2$, they require much higher actuation power. Therefore, $h_{\text{jet}}^+ = 2$ is studied in the main text.

B.2. *Jet-sheet velocity*

The maximum SJS velocity is changed between $U_{\text{jet,max}}^+ = 0$ and $U_{\text{jet,max}}^+ = 27$ and the drag-reduction margin is plotted in figure 24(b). The maximum drag-reduction margin $\mathcal{R} = 12.2\%$ is obtained for $U_{\text{jet,max}}^+ = 21.6$.

B.3. *Jet-sheet period of oscillation*

The effect of the actuation period is displayed in figure 25(a). For the tested cased, the maximum reduction is 19.4% for $T_{\text{osc}}^+ = 62.5$.
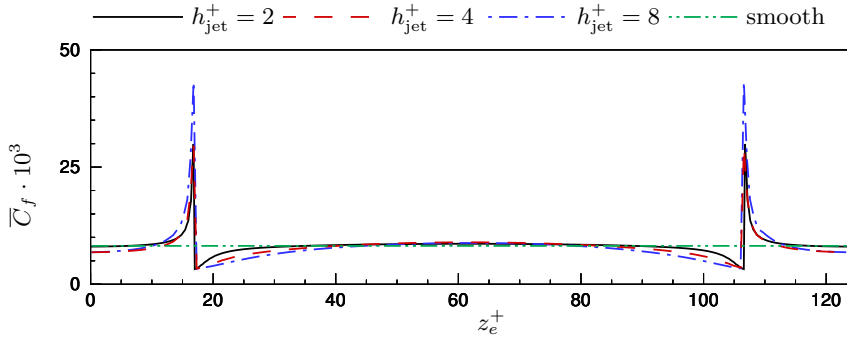
Figure 23: The time and spatial averaged skin-friction-coefficients along spanwise direction for different SJS heights for jet off cases.
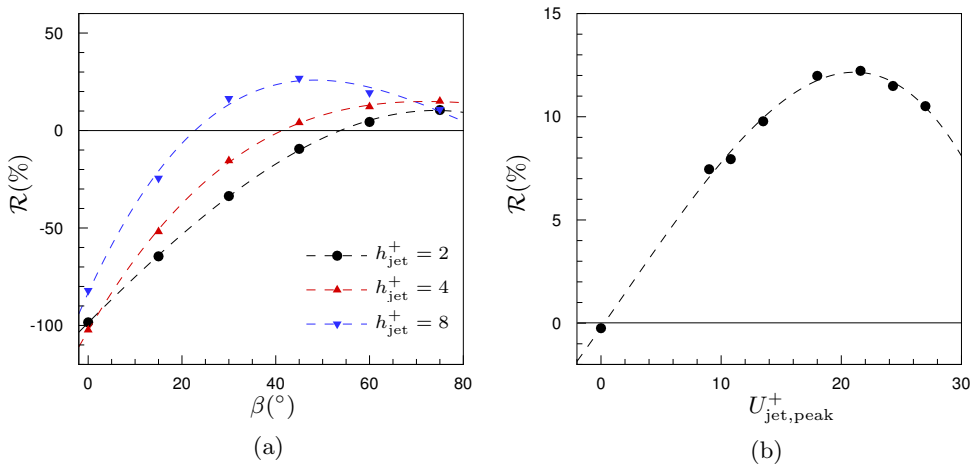

Figure 24: Drag reduction for different SJS slot heights (a) and SJS velocities (b).
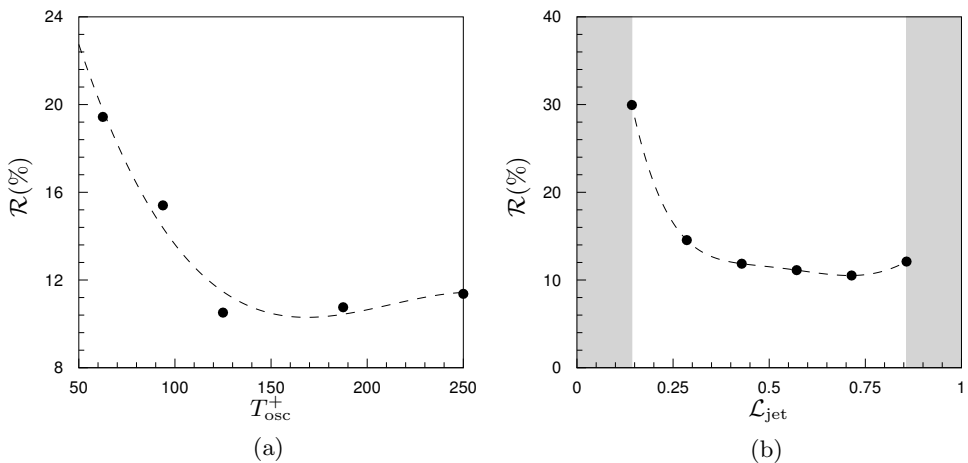

Figure 25: Drag reduction for different SJS periods (a) and lengths of jet walls (b).
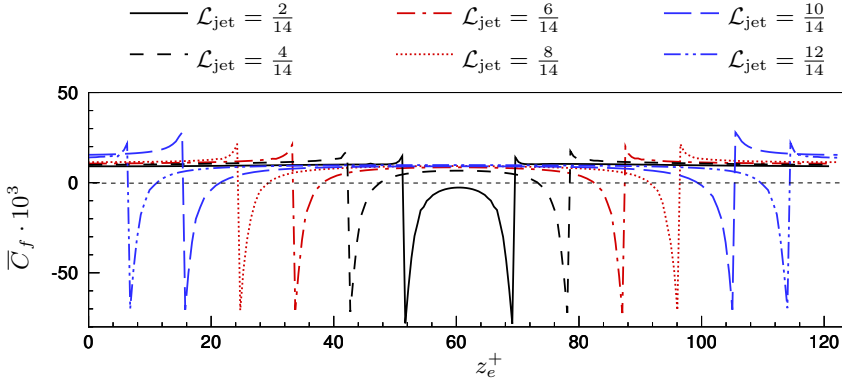
Figure 26: Comparison of time and spatially averaged skin-friction distribution along spanwise direction for different length ratios.

B.4. *Length of jet wall*

Different $\mathcal{L}_{\text{jet}} = L_{\text{jet}}^+/(L_{\text{step}}^+ + L_{\text{jet}}^+)$ are tested by using the same number of devices in the channel and the same dimensions of the computational domain. As shown in figure 25(b), values of $\mathcal{L}$ that are too close to 0 and 1 are not investigated. Values too close to 0 would not be realistic because the distance between SJS would be too small, while values too close to 1 would render L_{step}^+ too short because there would not be enough space for the vanes under the steps to generate the SJS. The largest drag-reduction margin is 30.0% for $\mathcal{L}_{\text{jet}} = 2/14$. The spanwise distribution of the skin-friction coefficient is plotted in figure 26 for different $\mathcal{L}_{\text{jet}}$ values. The friction drag is dramatically reduced on the jet wall for $\mathcal{L}_{\text{jet}} = 2/14$ because the SJS are very close to each other and interact. The other cases of different $\mathcal{L}_{\text{jet}}$ present almost the same drag-reduction margin on the jet wall. On the step wall, the friction drag is increased the most for $\mathcal{L}_{\text{jet}} = 10/14$.

Appendix C. Power balance in the cavity chambers

The integral power balance of air inside the two cavity chambers is derived herein (Panton 2013). The control volume is fixed in time and bounds the two cavity chambers, as shown in figure 13. We derive the integral mechanical power equation, the integral equation for the internal energy per unit time and then we sum these two equations to find the integral equation for the total power.

C.1. *Mechanical power in the cavity chambers*

We start by performing the scalar product of the velocity $\mathbf{u}$ and the compressible Navier-Stokes equations,

$$\rho \frac{D}{Dt}\left(\frac{|\mathbf{u}|^2}{2}\right) = -\mathbf{u} \cdot \nabla p + \frac{1}{Re_p}\mathbf{u} \cdot (\nabla \cdot \underline{\boldsymbol{\tau}}), \tag{C 1}$$

where D/Dt denotes the material derivative and $\underline{\boldsymbol{\tau}}$ is the stress tensor. By using vector and tensor identities, equation (C 1) is written as

$$\rho \frac{D}{Dt}\left(\frac{|\mathbf{u}|^2}{2}\right) = p(\nabla \cdot \mathbf{u}) - \nabla \cdot (p\mathbf{u}) + \frac{1}{Re_p}\nabla \cdot (\underline{\boldsymbol{\tau}} \cdot \mathbf{u}) - \frac{1}{Re_p}\underline{\boldsymbol{\tau}} : \nabla \mathbf{u}, \tag{C 2}$$

707 where the symbol : is the contraction. By using the continuity equation, the left-hand
708 side of equation (C 2) expands as follows,

$$\frac{\partial}{\partial t}\left(\rho\frac{|\mathbf{u}|^2}{2}\right) + \nabla\cdot\left(\rho\mathbf{u}\frac{|\mathbf{u}|^2}{2}\right) = p(\nabla\cdot\mathbf{u}) - \nabla\cdot(p\mathbf{u}) + \frac{1}{Re_p}\nabla\cdot(\boldsymbol{\tau}\cdot\mathbf{u}) - \frac{1}{Re_p}\boldsymbol{\tau}:\nabla\mathbf{u}. \quad \text{(C 3)}$$

709 Equation (C 3) is integrated over a control volume V and, by using the divergence
710 theorem, one finds

$$\int_V \frac{\partial}{\partial t}\left(\rho\frac{|\mathbf{u}|^2}{2}\right)\mathrm{d}V + \int_A \rho\frac{|\mathbf{u}|^2}{2}\mathbf{u}\cdot\mathbf{n}\mathrm{d}A = \int_V p(\nabla\cdot\mathbf{u})\mathrm{d}V - \int_A p\mathbf{u}\cdot\mathbf{n}\mathrm{d}A +$$
$$\frac{1}{Re_p}\int_A (\boldsymbol{\tau}\cdot\mathbf{u})\cdot\mathbf{n}\mathrm{d}A - \frac{1}{Re_p}\int_V \boldsymbol{\tau}:\nabla\mathbf{u}\mathrm{d}V, \quad \text{(C 4)}$$

711 where A is the surface of the control volume V and $\mathbf{n}$ is the unit vector pointing out of
712 the surface A. Using the Reynolds transport theorem, equation (C 4) is written as

$$\frac{\mathrm{d}}{\mathrm{d}t}\int_V \rho\frac{|\mathbf{u}|^2}{2}\mathrm{d}V = -\int_A \rho\frac{|\mathbf{u}|^2}{2}\mathbf{u}\cdot\mathbf{n}\mathrm{d}A - \int_A p\mathbf{u}\cdot\mathbf{n}\mathrm{d}A + \frac{1}{Re_p}\int_{A_{fluid}}(\boldsymbol{\tau}\cdot\mathbf{u})\cdot\mathbf{n}\mathrm{d}A +$$
$$\frac{1}{Re_p}\int_{A_{solid}}(\boldsymbol{\tau}\cdot\mathbf{u})\cdot\mathbf{n}\mathrm{d}A + \int_V p(\nabla\cdot\mathbf{u})\mathrm{d}V - \frac{1}{Re_p}\int_V \boldsymbol{\tau}:\nabla\mathbf{u}\mathrm{d}V, \quad \text{(C 5)}$$

713 where the term involving the stress tensor has been split into two terms, one involving
714 the shear stresses at the fluid part of A and one involving the shear stresses at the solid
715 part of A. The surface-integrated pressure-work term in (C 5) is split into two terms by
716 introducing the work per unit time that is exchanged by the fluid at the SJS apertures
717 and the work per unit time performed by the piston against the fluid pressure over the
718 piston area A_{piston}. The first term on the right-hand side of (C 5) simplifies because only
719 the fluid portion of A at the SJS apertures contributes to the balance. Equation (C 5)
720 becomes

$$\underbrace{\frac{\mathrm{d}}{\mathrm{d}t}\int_V \rho\frac{|\mathbf{u}|^2}{2}\mathrm{d}V}_{\mathrm{d}\mathcal{E}_m/\mathrm{d}t} = \underbrace{-\int_{A_{fluid}} p\mathbf{u}\cdot\mathbf{n}\mathrm{d}A}_{\mathcal{P}_{fluid}} - \underbrace{\int_{A_{fluid}} \rho\frac{|\mathbf{u}|^2}{2}\mathbf{u}\cdot\mathbf{n}\mathrm{d}A}_{\mathcal{F}_{m-fluid}} + \underbrace{\frac{1}{Re_p}\int_{A_{fluid}}(\boldsymbol{\tau}\cdot\mathbf{u})\cdot\mathbf{n}\mathrm{d}A}_{\mathcal{T}_{fluid}} +$$
$$\underbrace{\int_V p(\nabla\cdot\mathbf{u})\mathrm{d}V}_{\mathcal{C}} - \underbrace{\frac{1}{Re_p}\int_V \boldsymbol{\tau}:\nabla\mathbf{u}\mathrm{d}V}_{\mathcal{D}} - \underbrace{w_{\mathrm{piston}}(t)\int_{A_{piston}}\Delta p_{\mathrm{piston}}\mathrm{d}A}_{\mathcal{W}_{\mathrm{piston}}}. \quad \text{(C 6)}$$

721 The physical meaning of the terms in equation (C 6) is as follows,
722 • $\mathrm{d}\mathcal{E}_m/\mathrm{d}t$: time rate of change of the volume-integrated kinetic energy of the fluid
723 inside the control volume.
724 • $\mathcal{P}_{fluid}$: work per unit time performed by the fluid pressure as the fluid passes through
725 the SJS apertures.
726 • $\mathcal{F}_{m-fluid}$: flux of kinetic energy per unit time as the fluid passes through the SJS
727 apertures.
728 • $\mathcal{T}_{fluid}$: work per unit time performed by the fluid shear stresses as the fluid passes
729 through the SJS apertures.
730 • $\mathcal{C}$: work per unit time performed to compress the fluid.

731 • $\mathcal{D}$: dissipation per unit time of kinetic energy per unit time into heat due to viscous
732 shear stresses.
733 • $\mathcal{W}_{\text{piston}}$: work per unit time exerted by the piston to the fluid in the cavity chambers.

C.2. *Internal energy per unit time in the cavity chambers*

735 The equation of internal energy per unit time, from equation (5.10.3) in Panton (2013),
736 reads

$$\rho\frac{De}{Dt} = \frac{\partial(\rho e)}{\partial t} + \nabla\cdot(\rho\mathbf{u}e) = -p(\nabla\cdot\mathbf{u}) + \frac{1}{Re_p}\nabla\cdot(k\nabla\mathrm{T}) + \frac{1}{Re_p}\boldsymbol{\tau}:\nabla\mathbf{u}, \qquad (\text{C}7)$$

737 where $\rho e = \rho^* e^*/(\rho_c^* U_p^{*2})$ is the scaled internal energy per unit volume, $\mathrm{T} = \mathrm{T}^*/\mathrm{T}_c^*$ is the
738 temperature scaled by the reference temperature of the channel flow T_c^*, $k = k^*\mu_c^* U_p^{*2}/\mathrm{T}_c^*$
739 is the scaled thermal conductivity of air in the channel and μ_c^* is the reference dynamic
740 viscosity of air in the channel. The volume-integrated left-hand side of equation (C 7)
741 transforms as follows

$$\int_V \rho\frac{De}{Dt}\mathrm{d}V = \int_V \nabla\cdot(\rho\mathbf{u}e)\mathrm{d}V + \int_V \frac{\partial(\rho e)}{\partial t}\mathrm{d}V = \int_A \rho e\mathbf{u}\cdot\mathbf{n}\mathrm{d}A + \frac{\mathrm{d}}{\mathrm{d}t}\int_V \rho e\mathrm{d}V \qquad (\text{C}8)$$

742 by expanding the material derivative and by using the divergence and the Reynolds
743 transport theorem. By substituting (C 8) into the volume-integrated (C 7) and by using
744 the divergence theorem, one finds

$$\underbrace{\frac{\mathrm{d}}{\mathrm{d}t}\int_V \rho e\mathrm{d}V}_{\mathrm{d}\mathcal{E}_i/\mathrm{d}t} = -\underbrace{\int_{A_{fluid}} \rho e\mathbf{u}\cdot\mathbf{n}\mathrm{d}A}_{\mathcal{F}_{i-fluid}} - \underbrace{\int_V p(\nabla\cdot\mathbf{u})\mathrm{d}V}_{\mathcal{C}} +$$

$$\underbrace{\frac{1}{Re_p}\int_A k\nabla\mathrm{T}\cdot\mathbf{n}\mathrm{d}A}_{\mathcal{Q}} + \underbrace{\frac{1}{Re_p}\int_V \boldsymbol{\tau}:\nabla\mathbf{u}\mathrm{d}V}_{\mathcal{D}}. \qquad (\text{C}9)$$

745 The physical meaning of the terms in equation (C 9) is as follows,
746 • $\mathrm{d}\mathcal{E}_i/\mathrm{d}t$: time rate of change of the volume-integrated internal energy of the fluid
747 inside the control volume.
748 • $\mathcal{F}_{i-fluid}$: flux of internal energy per unit time as the fluid passes through the SJS
749 apertures.
750 • $\mathcal{Q}$: heat transfer through the surface of the control volume.

C.3. *Total power balance in the cavity chambers*

752 The balance equation for the integral total power, given by the sum of the integral
753 mechanical power and the internal energy per unit time, $\mathcal{E} = \mathcal{E}_m + \mathcal{E}_i$, is obtained by
754 adding (C 6) and (C 9).

$$\underbrace{\frac{\mathrm{d}}{\mathrm{d}t} \int_V \rho \left(e + \frac{|\mathbf{u}|^2}{2} \right) \mathrm{d}V}_{\mathrm{d}\mathcal{E}/\mathrm{d}t} = -\underbrace{\int_{A_{fluid}} p\mathbf{u} \cdot \mathbf{n}\mathrm{d}A}_{\mathcal{P}_{fluid}} - \underbrace{\int_{A_{fluid}} \rho e\mathbf{u} \cdot \mathbf{n}\mathrm{d}A}_{\mathcal{F}_{i-fluid}} -$$

$$\underbrace{\int_{A_{fluid}} \rho \frac{|\mathbf{u}|^2}{2} \mathbf{u} \cdot \mathbf{n}\mathrm{d}A}_{\mathcal{F}_{m-fluid}} - \underbrace{w_{\mathrm{piston}}(t) \int_{A_{piston}} \Delta p_{\mathrm{piston}}\mathrm{d}A}_{\mathcal{W}_{\mathrm{piston}}} + \underbrace{\frac{1}{Re_p} \int_{A_{fluid}} (\underline{\boldsymbol{\tau}} \cdot \mathbf{u}) \cdot \mathbf{n}\mathrm{d}A}_{\mathcal{T}_{fluid}} +$$

$$\underbrace{\frac{1}{Re_p} \int_A k\nabla \mathrm{T} \cdot \mathbf{n}\mathrm{d}A}_{\mathcal{Q}} \tag{C 10}$$

The compression term $\mathcal{C}$ and the dissipation term $\mathcal{D}$ cancel out because they both appear in (C 6) and (C 9) with opposite signs.

REFERENCES

Baron, A. & Quadrio, M. 1996 Turbulent drag reduction by spanwise wall oscillations. *Appl. Sc. Res.* **55**, 311–326.

Bewley, T. R., Moin, P. & Temam, R. 2001 DNS-based predictive control of turbulence: An optimal benchmark for feedback algorithms. *J. Fluid Mech.* **447**, 179–225.

Cannata, M., Cafiero, G. & Iuso, G. 2020 Large-scale forcing of a turbulent channel flow through spanwise synthetic jets. *AIAA J.* **58** (5), 2042–2052.

Cannata, M. & Iuso, G. 2008 Spanwise directed synthetic jets for wall turbulence control. In *AIAA Paper 2008-4205*, p. 4205.

Choi, K.-S., DeBisschop, J.R. & Clayton, B.R. 1998 Turbulent boundary-layer control by means of spanwise-wall oscillation. *AIAA J.* **36** (7), 1157–1162.

Chung, Y..M & Talha, T. 2011 Effectiveness of active flow control for turbulent skin friction drag reduction. *Phys. Fluids* **23** (2), 025102.

Corke, T.C. & Thomas, F.O. 2018 Active and passive turbulent boundary-layer drag reduction. *AIAA J.* **56** (10), 3835–3847.

Glezer, A. & Amitay, M. 2002 Synthetic jets. *Ann. Rev. Fluid Mech.* **34** (1), 503–529.

Hehner, M.T., Gatti, D. & Kriegseis, J. 2019 Stokes-layer formation under absence of moving parts - A novel oscillatory plasma actuator design for turbulent drag reduction. *Phys. Fluids* **31** (5), 051701.

Hehner, M.T., Gatti, D., Mattern, P., Kotsonis, M. & Kriegseis, J. 2020 Virtual wall oscillations forced by a dbd plasma actuator operating under beat frequency-a concept for turbulent drag reduction. In *AIAA Aviation 2020 Forum*, p. 2956.

Hwang, H.G. & Lee, J.H. 2018 Secondary flows in turbulent boundary layers over longitudinal surface roughness. *Phys. Rev. Fluids* **3** (1), 014608.

Iuso, G. & Di Cicca, G.M. 2007 Interaction of synthetic jets with a fully developed turbulent channel flow. *J. Turbul.* **8**, N11.

Iuso, G., Onorato, M., Spazzini, P.G. & di Cicca, G.M. 2002 Wall turbulence manipulation by large-scale streamwise vortices. *J. Fluid Mech.* **473**, 23–58.

Jeong, J. & Hussain, F. 1995 On the identification of a vortex. *J. Fluid Mech.* **285**, 69–94.

Jung, W.J., Mangiavacchi, N. & Akhavan, R. 1992 Suppression of turbulence in wall-bounded flows by high-frequency spanwise oscillations. *Phys. Fluids A* **4** (8), 1605–1607.

Kim, J., Moin, P. & Moser, R. 1987 Turbulence statistics in fully developed channel flow at low Reynolds number. *J. Fluid Mech.* **177**, 133–166.

Kim, K.H. & Kim, C. 2005 Accurate, efficient and monotonic numerical methods for multi-dimensional compressible flows: Part I: Spatial discretization. *J. Comp. Phys.* **208** (2), 527–569.

Lindgren, B., Österlund, J. & Johansson, A.V. 1998 Measurement and calculation of guide vane performance in expanding bends for wind-tunnels. *Exp. Fluids* **24** (3), 265–272.

PANTON, R. 2013 *Incompressible Flow*. Wiley-Interscience – Fourth Edition.

QIN, N. & XIA, H. 2008 Detached eddy simulation of a synthetic jet for flow control. *Proc. Inst. Mech. Eng., Part I: J. Syst. Control Eng.* **222** (5), 373–380.

QUADRIO, M. & RICCO, P. 2004 Critical assessment of turbulent drag reduction through spanwise wall oscillations. *J. Fluid Mech.* **521**, 251–271.

QUADRIO, M. & RICCO, P. 2011 The laminar generalized Stokes layer and turbulent drag reduction. *J. Fluid Mech.* **667**, 135–157.

QUADRIO, M., RICCO, P. & VIOTTI, C. 2009 Streamwise-travelling waves of spanwise wall velocity for turbulent drag reduction. *J. Fluid Mech.* **627**, 161–178.

RICCO, P., SKOTE, M. & LESCHZINER, M.A. 2021 A review of turbulent skin-friction drag reduction by near-wall transverse forcing. *Progr. Aero. Sc.* **123**, 100713.

SAHLIN, A. & JOHANSSON, A.V. 1991 Design of guide vanes for minimizing the pressure loss in sharp bends. *Phys. Fluids* **3** (8), 1934–1940.

STROH, A., FROHNAPFEL, B., SCHLATTER, P. & HASEGAWA, Y. 2015 A comparison of opposition control in turbulent boundary layer and turbulent channel flow. *Phys. Fluids* **27** (7), 075101.

TAY, C.M.J., HERBERG, M., ONORATO, M. & TSAI, H.M. 2007 Effect of traversal jet injections on skin friction in a turbulent channel. In *45th AIAA Aero. Sc. Meeting and Exhibit*, , vol. AIAA-323.

THOMAS, F.O., CORKE, T.C., DUONG, A., MIDYA, S. & YATES, K. 2019 Turbulent drag reduction using pulsed-DC plasma actuation. *J. Phys. D: Applied Phys.* **52** (43), 434001.

VANDERWEL, C. & GANAPATHISUBRAMANI, B. 2015 Effects of spanwise spacing on large-scale secondary flows in rough-wall turbulent boundary layers. *J. Fluid Mech.* **774** (R2).

VANDERWEL, C., STROH, A., KRIEGSEIS, J., FROHNAPFEL, B. & GANAPATHISUBRAMANI, B. 2019 The instantaneous structure of secondary flows in turbulent boundary layers. *J. Fluid Mech.* **862**, 845–870.

WEISS, J.M. & SMITH, W.A. 1995 Preconditioning applied to variable and constant density flows. *AIAA J.* **33** (11), 2050–2057.

YAO, J., CHEN, X. & HUSSAIN, F. 2018 Drag control in wall-bounded turbulent flows via spanwise opposed wall-jet forcing. *J. Fluid Mech.* **852**, 678–709.

YOU, D., WANG, M. & MOIN, P. 2006 Large-eddy simulation of flow over a wall-mounted hump with separation control. *AIAA J.* **44** (11), 2571–2577.

ZHOU, D. & BALL, K.S. 2008 Turbulent drag reduction by spanwise wall oscillations. *Int. J. Eng. Trans. A Basics* **21** (1), 85–104.